Modeling spectral and total solar irradiance variability from any vantage point in the Solar System

Dissertation
for the award of the degree

"Doctor rerum naturalium" (Dr.rer.nat.)

of the Georg-August-Universität Göttingen

within the doctoral program "Physics"
of the Georg-August University School of Science (GAUSS)

submitted by

Isabela de Oliveira Martins

from São Paulo, Brazil

Göttingen, 2024

Thesis Committee

Dr. Alexander Shapiro
Max Planck Institute for Solar System Research, Göttingen, Germany

Prof. Dr. Laurent Gizon
Max Planck Institute for Solar System Research, Göttingen, Germany
Institute for Astrophysics and Geophysics, Georg-August-Universität Göttingen

Prof. Dr. Stefan Dreizler
Institute for Astrophysics and Geophysics, Georg-August-Universität Göttingen

Members of the Examination Board

Reviewer: Prof. Dr. Laurent Gizon
Max Planck Institute for Solar System Research, Göttingen, Germany
Institute for Astrophysics and Geophysics, Georg-August-Universität Göttingen

Second Reviewer: Prof. Dr. Stefan Dreizler
Institute for Astrophysics and Geophysics, Georg-August-Universität Göttingen

Further members of the Examination Board:

Prof. Dr. Ariane Frey
II. Institute of Physics, Georg-August-Universität Göttingen

Dr. Natalie Krivova
Max Planck Institute for Solar System Research, Göttingen, Germany

Dr. Joanna Drążkowska
Max Planck Institute for Solar System Research, Göttingen, Germany

PD Dr. Olga Shishkina
Max Planck Institute for Dynamics and Self-Organization, Göttingen, Germany

Date of the oral examination: 25.09.2024

Printed in Germany

DOI: 10.53846/goediss-10832

Contents

Summary

The Sun is the primary external energy source for all planets in the Solar System. Its radiative flux, known as solar irradiance, plays a crucial role in planetary atmosphere modeling. Accurate spectral solar irradiance (SSI) measurements are essential for understanding the temperature, composition, and dynamics of planetary atmospheres, as well as their climate and weather patterns. Climate models depend on accurate SSI data to simulate solar forcing effects. Measurements of SSI at Earth are available from spacecraft missions, but similar data for other planets are limited. Mars is the only planet with SSI measurements, obtained by the Mars Atmosphere and Volatile EvolutioN spacecraft. The lack of SSI measurements for other planets hinders the study of solar influence on planetary atmospheres and climate.

To address this gap, my dissertation proposes to use information about magnetic activity on both the near and far sides of the Sun to estimate solar irradiance variability from any vantage point in the Solar System. Near side measurements are obtained through direct observations, while far side information is derived from helioseismic holography. Far side information can also be obtained by using a surface flux transport model. This comprehensive approach enables sufficiently accurate irradiance variability estimations for planetary studies using the Spectral And Total Irradiance REconstruction (SATIRE) model, which attributes irradiance variations over periods longer than a day to the emergence and evolution of solar surface magnetic features – i.e., sunspots and faculae. Irradiance is then calculated as the sum of contributions from the quiet Sun and these magnetic features. Others have also addressed this gap by interpolating Earth-based irradiance measurements and scaling them according to the Sun-planet distance in order to estimate solar irradiance variability at other planets. However, this interpolation approach overlooks the inherent solar irradiance variability over various timescales and the evolution of solar surface magnetic fields.

The estimation of solar irradiance variability relies on area coverage calculations of magnetic features. In Chapter 2, synthetic full surface magnetograms generated by a Surface Flux Transport Model are converted into sunspots and faculae areas, and the wavelength-integrated spectral irradiance (total solar irradiance, or TSI) and the S-index (a proxy for ultraviolet irradiance variability) are calculated. The results demonstrate that simple phase-shifted Earth-based irradiance measurements are unreliable for other planets due to the dynamic nature of sunspots and faculae. The study finds agreement in S-index variability between the traditional interpolation method and the new approach, since this variability is dominated by faculae, which have longer lifetimes and cover a larger portion of the solar surface. However, significant discrepancies are observed in TSI variability estimates, particularly because sunspots, which are short-lived magnetic features that dominate the TSI variability, are not adequately captured by the interpolation approach. This finding highlights the limitations of an interpolation method that disregards far side solar activity.

Chapter 3 builds on the previous chapter by addressing the challenge of estimating solar irradiance variability with limited data from the far side of the Sun. High-resolution magnetograms and continuum intensity images used for Earth-based irradiance reconstruction are unavailable for the far side, and therefore, magnetic field data alone must suffice. Here, I use Far side Active Region Magnetograms (FARM) – which are derived from far side seismic images – to estimate the area coverage of sunspots and faculae on the far side of the Sun. The results show that magnetic field data can serve as a reliable proxy for the area coverage of sunspots and faculae, enabling the estimation of solar irradiance variability at different positions in the ecliptic plane. The estimates are not as accurate as those obtained from the SATIRE model, but they provide a more reliable alternative to the interpolation method when near side data are unavailable.

Chapter 1

Introduction

1.1 Motivation

The Sun is the primary source of external energy for the planetary atmospheres in the Solar System. The solar spectrum and its variations influence the temperature, the composition, and the dynamics of the atmospheres, as well as the climate and the weather patterns on the planets (Gray et al. 2010). There are several models in the literature that are used to study the Earth's climate system and to predict future climate scenarios under different conditions (e.g., Buehler et al. 2018; Hohenegger et al. 2023). One of the important input parameters for these models is the solar irradiance, which is used to simulate the effects of solar forcing on Earth's atmosphere.

The Earth system, however, should not be taken as the only example of how solar irradiance influences planetary atmospheres. The other planets in the Solar System have different atmospheric compositions, temperatures, and dynamics, which are also influenced by the solar irradiance (e.g., Almatroushi et al. 2021; Haberle et al. 2019). Analogously to the Earth case, an essential input parameter in the models used to study the atmospheres of other planets is the incoming solar irradiance at that planet. But how is this parameter estimated in other positions of the Solar System?

While measurements of spectral solar irradiance and its variability have been successfully obtained from Earth's vantage point through spacecraft missions (e.g., Harder et al. 2005; Fröhlich et al. 1997; Snow et al. 2005), similar measurements at other planets are still lacking. Currently, the only mission that has provided such measurements at another planet is the Mars Atmosphere and Volatile EvolutioN (MAVEN, Jakosky et al. 2015) spacecraft. Since 2014, MAVEN has been monitoring the solar extreme ultraviolet irradiance at Mars. However, these measurements are limited to specific wavelengths and are not available for other planets in the Solar System.

In order to estimate the solar irradiance at other planets, researchers often rely on measurements made at Earth. The common approach involves interpolating Earth-based measurements and scaling them based on the Sun-planet distance (Thiemann et al. 2017). However, this approach disregards solar irradiance's inherent variability over various timescales, including how the solar surface evolves due to the presence of magnetic features, and the emergence and distribution of these features.

The aim of the research presented in this dissertation is to reduce the reliability on Earth-based measurements for estimating solar irradiance at any point in the Solar System. This is achieved by utilizing measurements and estimations of magnetic fields on the solar surface, both on the near and on the far side of the Sun – i.e., the solar hemisphere facing and hidden from Earth, respectively.

On the near side of the Sun, measurements of magnetic fields can be obtained by direct observations (Schou et al. 2012). On the far side of the Sun, information about magnetically active regions are derived from products of helioseismic holography (Yang et al. 2023) combined with a surface flux transport model (Baumann 2005). The combination of these two datasets covers the entire solar surface and allows for the estimation of the solar irradiance at any point in the Solar System.

The method used in this work to estimate solar irradiance is based on the Spectral And Total Irradiance REconstruction (SATIRE, Fligge, Solanki, and Unruh 2000; Krivova et al. 2003) model, which is based on the fact that variations in solar irradiance, occurring over time periods longer than a day, arise exclusively from the presence of magnetic fields in the solar surface. The irradiance is then calculated as the sum of the contributions from the quiet Sun and from the surface magnetic features.

This dissertation is organized as follows. In the following sections of Chapter 1, I provide the basic concepts associated with solar irradiance and its variability. I also give an overview of the role of solar irradiance and its variability in defining the properties of planetary systems. In Chapter 2, I discuss the common interpolation approach to estimating solar irradiance at other planets and how it compares to the results from the SATIRE-inspired model. In Chapter 3, I present the method used to calculate the area coverage of magnetic features on the far side of the Sun, and how the irradiance estimations compare to real measurements from Mars. Finally, in Chapter 4, I discuss the current status of the work and the implications of the findings.

1.2 Spectral and total solar irradiance

The solar irradiance is the radiative flux emitted by the Sun. This flux propagates radially throughout the Solar System, with a total power output of about 3.8×10^{26} W (Solanki, Krivova, and Haigh 2013). The total solar irradiance (TSI, measured in $\mathrm{W\,m^{-2}}$) is defined as the total power output of the Sun per unit area at a distance of 1 au from the Sun. The TSI is the wavelength-integrated spectral solar irradiance (SSI, measured in $\mathrm{W\,m^{-2}\,nm^{-1}}$). When integrated over all wavelengths, the TSI is approximately $1361\,\mathrm{W\,m^{-2}}$ at the top of Earth's atmosphere during solar minimum (Kopp and Lean 2011). This value is known as the "solar constant" and is used as a reference for TSI measurements, although it is not truly constant, as explained in Section 1.4.

The solar electromagnetic spectrum is similar to that of a black body with a temperature of about 5800 K (Liou 2002). Most of the irradiance is emitted in the visible (VIS) and in the infrared (IR) ranges, originating from the visible surface of the Sun – the photosphere. The next large contribution to the spectrum comes from the ultraviolet (UV) region, which is dominated by emissions from the solar atmosphere regions above the photosphere – the chromosphere and the transition region. Emissions in the X-ray and the radio regions are originated in the solar corona – the outermost layer of the solar atmosphere.

1.3 Sunspots, faculae, and the quiet Sun

The photosphere of the Sun is home to various magnetic features of different shapes, sizes and magnetic field strength. These surface manifestations of emerging magnetic fields are key components in the variability of solar irradiance, as explained later in Section 1.4. Unruh, Solanki, and Fligge (1999) show that a three-component model of the solar irradiance, which includes contributions from sunspots, faculae, and the non-variable quiet Sun, is sufficient to reproduce the observed variability of SSI. This section provides an overview of these three components (see Solanki, Krivova, and Haigh 2013 and references therein).

First of all, I introduce the concept of the quiet Sun. The quiet Sun is the region of the solar surface that is free from any visible manifestations of magnetic activity. It is characterized by its smooth appearance and relatively low levels of magnetic field intensity and brightness variability. The quiet Sun is the baseline for solar irradiance, against which the contributions of magnetic features are measured.

Sunspots are dark, cooler regions on the surface of the Sun that are associated with strong magnetic fields. They can vary in size, with diameters reaching up to 60 000 km. Their lifetime increases linearly with maximum size, which means they can live for a few hours up to months. They are characterized by their dark central region, known as the umbra, surrounded by a lighter region called the penumbra. In their center, the magnetic field is vertical, and it becomes gradually more horizontal towards its edges (Solanki, Inhester, and Schüssler 2006).

Sunspots often appear in regions of very strong magnetic fields, known as active regions, and are typically found near the equator of the Sun. They commonly appear in pairs with opposite magnetic polarity, where one sunspot has a positive polarity and the other has a negative polarity (Hale et al. 1919).

Bright magnetic features are also present on the solar surface. Faculae are hotter regions with smaller dimensions than sunspots. They can live up for several months and are associated with the presence of strong magnetic fields (Foukal and Lean 1988), being often found in the surroundings of sunspots as a large bright feature. Network of bright points are small, bright magnetic features that are scattered across the solar surface. In this work, I will refer to the bright features collectively as faculae, for the sake of simplicity.

Figure 1.1 provides a visual representation of sunspots and faculae on the Sun, captured on January 9th, 2014, by the Helioseismic and Magnetic Imager (HMI, Schou et al. 2012) and the Atmospheric Imaging Assembly (AIA, Lemen et al. 2012) instruments onboard the Solar Dynamics Observatory (SDO, Pesnell, Thompson, and Chamberlin 2012). The regions which are free from sunspots and faculae are what it is considered the quiet Sun.

In the left panel of Figure 1.1, a continuum intensity image of the solar photosphere in a broad VIS range reveals the presence of dark sunspots. The middle panel shows the photosphere – as well as the chromosphere and the transition region – in the UV bands at 1600 Å and 1700 Å, highlighting the bright faculae surrounding the sunspots. The right panel displays a line-of-sight magnetogram, where black and white patches indicate strong magnetic fields with opposite polarities. It is worth noting the presence of intense magnetic fields associated with both sunspots and faculae regions.

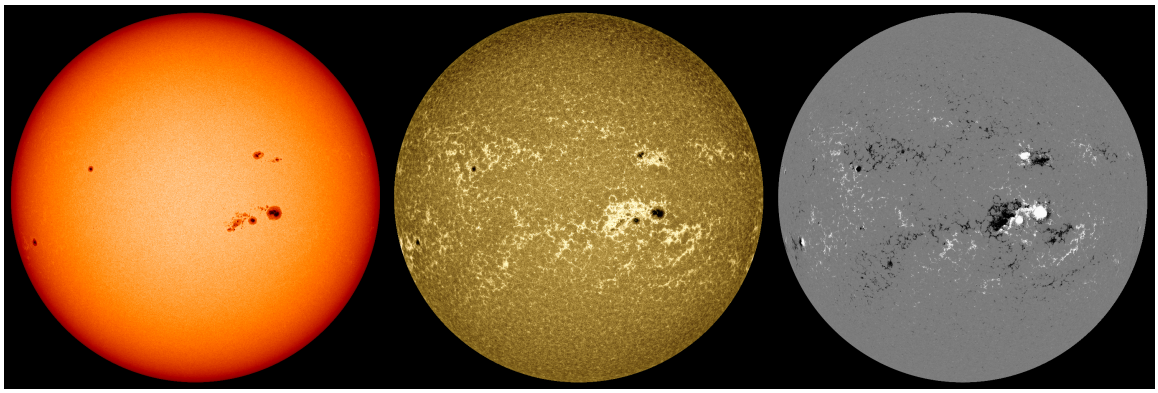

Figure 1.1: Solar disc observed by instruments onboard the SDO spacecraft, on January 9th, 2014. Left: Continuum intensity image, observed by HMI. Middle: Composite image from the 1600 Å and 1700 Å channels, observed by AIA. Right: Line-of-sight magnetogram, observed by HMI. I used the JHelioviewer software (Müller et al. 2017) to create the images.

Both sunspots and faculae are formed by the emergence of magnetic flux tubes from the solar interior. Flux tubes are cylindrical plasma structures, in which the magnetic field moves along with the plasma – i.e., is "frozen-in" to the fluid. As explained by Solanki, Krivova, and Haigh (2013), when these flux tubes reach the solar surface, they form different magnetic features, depending basically on their size.

The strong magnetic fields within both small and large magnetic flux tubes reduce the convective energy flux, leading to cooling of the magnetic features. The magnetic pressure within these flux tubes leads to their depression into the hotter subsurface layers of the Sun – the so called Wilson effect. The radiation from these surrounding layers heats up the flux tubes which are narrower than about 250 km, making them appear brighter than the surrounding photosphere, which is the case of the faculae (Spruit 1976; Keller et al. 2004). This effect is often referred to as heating from the hot walls. For flux tubes with larger diameter, the radiation only penetrates a small part of the volume, causing them to appear dark instead, which is the case of the sunspots (Rempel and Schlichenmaier 2011).

1.4 Solar irradiance variability

The solar irradiance is not constant, but it varies at all wavelengths and on all timescales that have been studied so far. In this section, I give an overview of the variability over the different timescales that are associated with the solar magnetic field, focusing on the TSI and on the UV, the VIS, and the near-IR wavelength bands.

Sunspots and faculae are directly associated with the solar activity cycle. This cycle is characterized by the variation in the number of magnetic features on the photosphere with a period of about 11 years. The cycle begins with a solar minimum, during which the number of magnetic features is at its lowest, and the latitudes of emergence of sunspots is approximately $\pm 30°$. As the cycle progresses, the number of magnetic features increases, reaching its peak at the solar maximum. By then, the latitude of emergence of sunspots decreases until they reach about $\pm 5°$ (Solanki, Inhester, and Schüssler 2006). Subsequently, the number of magnetic features decreases, leading to a new solar minimum and the initiation of a new cycle, characterized by the reversal of the magnetic polarity of sunspots in both solar hemispheres. The solar cycles can be observed in the form of butterfly diagrams, which show the latitudinal distribution of sunspots as a function of time.

Sunspots and faculae contribute to the variability of solar irradiance in different ways. Sunspots are generally associated with the decrease of irradiance, as their dark appearance reduces the amount of light emitted from the Sun. The variability due to sunspots is more pronounced in the VIS and near-IR regions of the spectrum. On the other hand, bright faculae generally contribute to an increase in irradiance (Foukal and Lean 1988). The variability due to faculae is more significant in the UV region.

The combined effect of sunspots and faculae leads to a net increase in TSI of around 0.1 % during periods of high solar activity (Fröhlich and Lean 1998). This implies that the variability of the TSI over the solar activity cycle is dominated by the effects of faculae (Shapiro et al. 2016), since these bright features have longer life times and cover a much larger portion of the solar surface than sunspots (Solanki, Krivova, and Haigh 2013).

Figure 1.2 shows the TSI measured by several instruments for the period between 1978 and 2024 (colorful curves), as well as the monthly sunspots number observed on the solar surface (black dots), approximately covering the solar cycles 21 to 25. The modulation of about 11 years is evident in the figure, with the peaks and valleys in the TSI corresponding to those of the monthly sunspot number. The peaks in the sunspot number correspond to periods of high solar activity, while the valleys correspond to periods of low solar activity.

Figure 1.3 shows the variability of the SSI in the UV (categorized in soft X-rays, XUV, extreme ultraviolet, EUV, and simply ultraviolet, UV), VIS, and near-IR regions over a period of 16 years. The variability of VIS and near-IR wavelength ranges can reach up to 0.5 % and it is mostly out-of-phase with the solar cycle. In contrast, the variability of the UV region is much larger, reaching as high as several tens of percent for wavelengths below 200 nm (Floyd et al. 2003), while mostly in-phase with the solar cycle.

The variability on timescales below five days is attributed to the emergence and evolution of magnetic features on the solar surface (see Figure 8 of Nèmec et al. 2020). Sunspots and faculae are constantly forming, evolving, and decaying. An observer traveling around the Sun in the same speed as the solar rotation – i.e., always looking at the same solar disc – would see a continuous change in the size and shape of magnetic features, leading to a continuous change in solar irradiance.

On the timescales between five days and a solar rotation, the variability is mainly attributed to the rotation itself and the consequent transits of magnetic features through the visible solar disc (Nèmec et al. 2020). As the Sun rotates and the magnetic features emerge, evolve and decay, the distribution of sunspots and faculae on the solar surface changes, considering an observer fixed in space. This leads to an anisotropic distribution of solar irradiance, with different regions of the solar disc emitting different amounts of light, also depending on the wavelength.

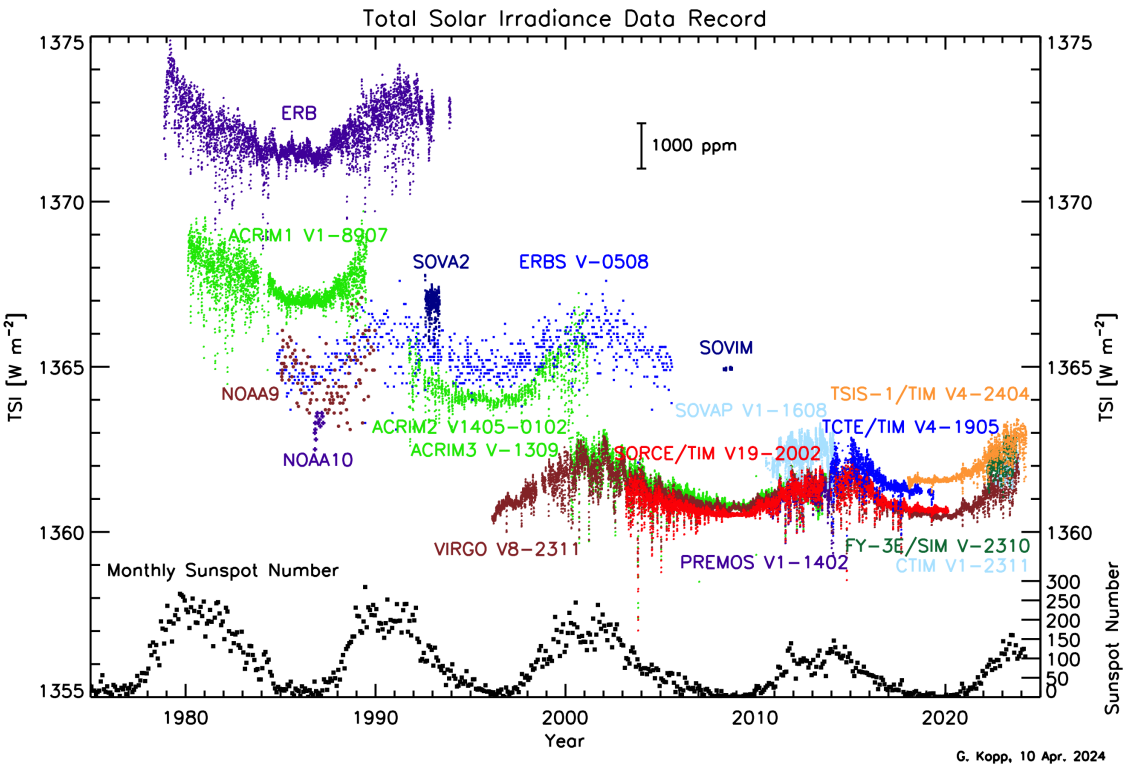

Figure 1.2: TSI measurements from several instruments for the period between 1978 and 2024 (in colors) and the monthly sunspot number (black dots) observed on the solar surface since the 1970s. It is important to note that the several instruments are calibrated differently, which leads to differences in the absolute values of the TSI. Courtesy of G. Kopp (https://spot.colorado.edu/~koppg/TSI/).

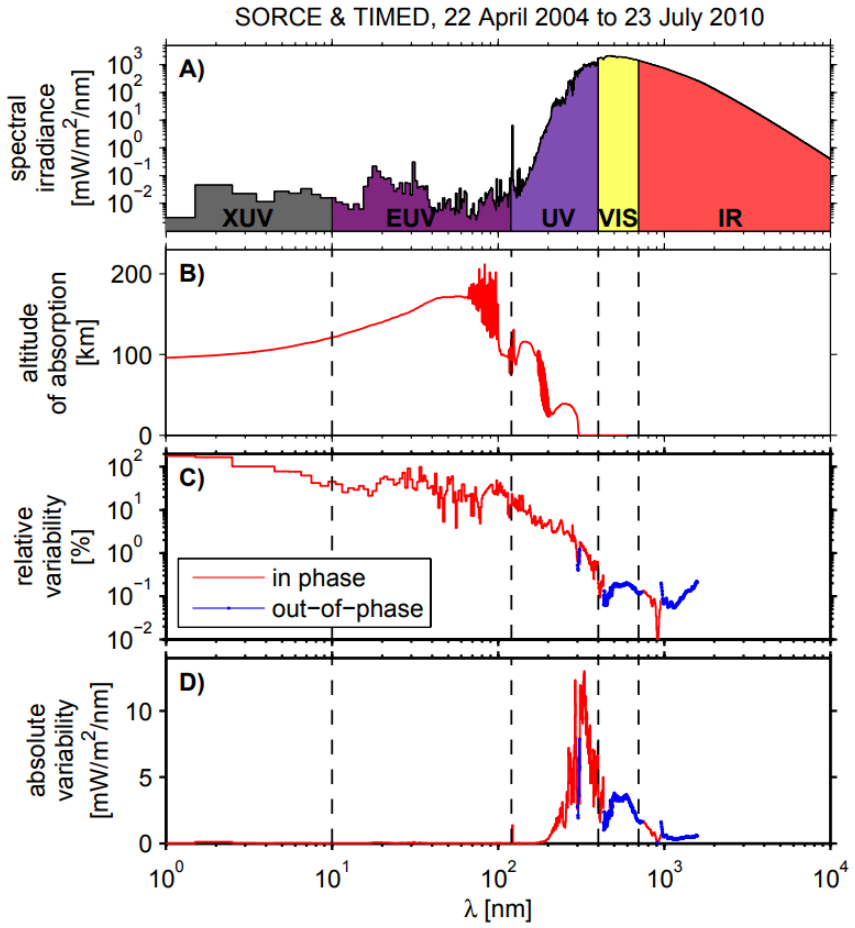

Figure 1.3: The SSI as inferred from observations by the SOlar Radiation and Climate Experiment (SORCE) and the Thermosphere Ionosphere Mesosphere Energetics and Dynamics (TIMED) missions, from April 2004 until July 2010. **A)** Average SSI for the period, segmented in soft X-ray (XUV), extreme ultraviolet (EUV), ultraviolet (UV), visible (VIS), and near-infrared (IR). **B)** Characteristic altitude of absorption of each wavelength in the Earth's atmosphere. **C)** Relative variability (peak-to-peak/average) for solar cycle variations. **D)** Absolute variability. Image credit: Ermolli et al. (2013), distributed under the Creative Commons Attribution 3.0 License.

A sub-effect of the variability due to solar rotation is the center-to-limb variations of the faculae. These are contrast variations caused by the angle of observation of a facula at different heliocentric angles – which is the angle between the line-of-sight and the surface normal. An example is illustrated in Figure 1.4, which shows an active region observed in the VIS range at the center and at the limb of the solar disc. In this wavelength region, the contrast between faculae and the background is enhanced at large heliocentric angles – i.e., towards the limb of the solar disc. Faculae usually appear brighter at the limb because of the angle of observation, since the hot walls of the faculae flux tubes are more visible when looking at the solar surface "from the side" (Steiner 2005).

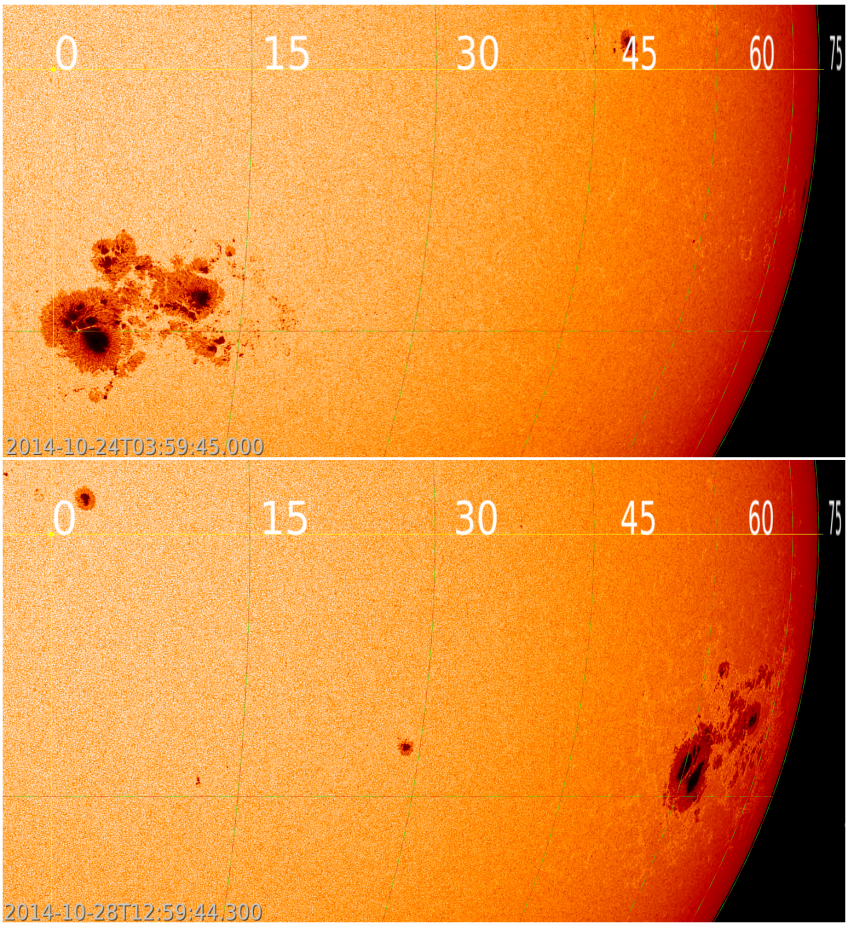

Figure 1.4: Continuum image of the solar photosphere showing the center-to-limb variations of active region NOAA AR12192. Top: Active region at the center of the solar disc. Bottom: The same active region at the limb of the solar disc. A longitude grid is overlaid on the images to show the orientation of the solar disc. I used the JHelioviewer software (Müller et al. 2017) to create the images.

1.5 Solar irradiance as the primary external source of planetary chemistry and composition

Solar irradiance is the main external source of energy for Earth's atmosphere. It plays a critical role in the dynamics and behavior of the atmosphere – see e.g. review by Gray et al. 2010 on solar influences on climate. Understanding the effects of solar forcing on Earth's atmosphere is essential for comprehending the climate system and forecasting weather patterns.

Depending on the wavelength, the incoming solar energy is either reflected back to space, absorbed by the atmosphere, or absorbed by the Earth's surface. Figure 1.5 shows the solar electromagnetic spectrum at the top of Earth's atmosphere (yellow region) – i.e., before any interaction with the atmosphere – and at Earth's surface (orange region). Notice that a large amount of the incoming radiation in the UV, the VIS, and the near-IR regions is absorbed by ozone, oxygen, and water vapor before reaching the surface.

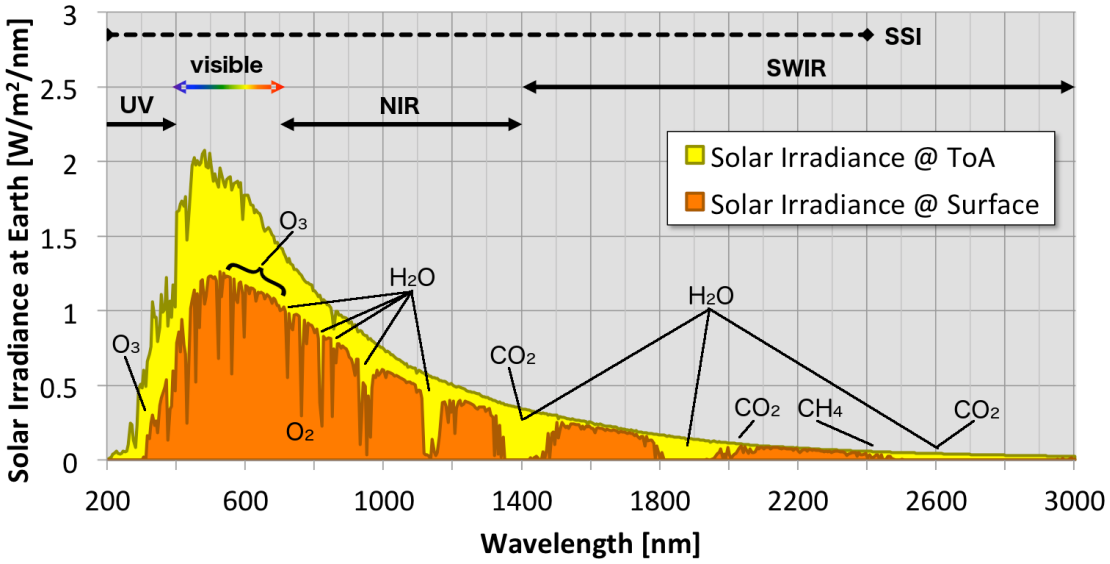

Figure 1.5: Simulated representation of the solar spectrum at the top of the atmosphere (ToA) and at Earth's surface. The spectral regions are: ultraviolet (UV), visible, near-infrared (NIR), and shortwave infrared (SWIR). The broken line at the top indicates the range typically covered by SSI. The regions of absorption of irradiance by various atmospheric constituents are labeled, including ozone (O_3), oxygen (O_2), water vapor (H_2O), carbon dioxide (CO_2), and methane (CH_4). Image credit: L. Ellison (https://sunclimate.gsfc.nasa.gov/article/solar-irradiance).

Figure 1.3 from Section 1.4 can also be discussed in terms of the altitude at which solar radiation is absorbed in the Earth's atmosphere. Irradiance in the XUV and EUV regions, which correspond to short and highly energetic wavelengths, is primarily absorbed above 100 km in the thermosphere where the ionosphere is located. The absorption of XUV and EUV radiation by the ionosphere has significant implications for the composition and dynamics of this region. Since the irradiance at these wavelengths exhibits large variations, the ionosphere experiences corresponding variations in composition and dynamics (Ermolli et al. 2013).

The purpose of this section is not to explain in details the reactions of the Earth system to solar radiation, but to emphasize the wide range of effects promoted by the incoming solar energy. A few examples of these effects – not only pertaining the atmosphere, but also the surface – studied in the literature (e.g., Ermolli et al. 2013; Lean 1997; Peixoto and Oort 1992) are:

- **Ionospheric layers** – The ionization of the upper atmosphere by EUV radiation leads to the formation of the ionosphere, in which the propagation of radio waves, the formation of auroras, and the distribution of electric currents in the atmosphere happen;
- **Atmospheric temperature** – The absorption of sunlight by atmospheric constituents heats the atmosphere, creating temperature gradients that drive atmospheric circulation, dictating short-term weather variations;
- **Ozone layer** – The UV radiation defines the photochemistry of the ozone formation and, consequently, the structure of the ozone layer, which protects life on Earth from the damaging effects of sunlight;
- **Surface temperature** – The differential heating of the Earth's surface by solar radiation – due to the spherical shape of Earth – also leads to the formation of pressure systems, such as high and low-pressure areas, which further influence the movement of air masses;
- **Water cycle** – The evaporation of water from the Earth's surface, driven by solar heating, is responsible for the formation of clouds and precipitation, which are essential for the distribution of water across the planet;
- **Photosynthesis** – Plants absorb solar radiation in the VIS and near-IR regions in order to produce energy through photosynthesis, which is the basis of the food chain on Earth.

Comparably, the solar irradiance also plays a key role in shaping the planetary systems in the Solar System. Some examples that have been studied in the literature (e.g. Catling 2015; Clancy et al. 2000) are:

- **Venus** – The sunlight absorption by the atmosphere lead to changes in the speed of Venus's zonal winds, which vary in agreement with the solar cycle;
- **Mars** – The Martian dust storms tend to occur when Mars is closest to the Sun – i.e., when the incoming solar radiation is larger – and have been shown to increase global temperature;
- **Titan** – The solar radiation is the primary driver for the formation of the haze in Titan's atmosphere, which is responsible for the moon's orange appearance.

Such effects are not only relevant for understanding the past and present conditions of the planets in the Solar System, but also for predicting their future evolution under different conditions. In order to accurately understand these effects, models that can estimate the spectral solar irradiance at any point in the Solar System are needed. This is the motivation behind the research presented in this dissertation.

Chapter 2

Estimation of spectral solar irradiance in the ecliptic plane using synthetic solar surface magnetograms

This chapter faithfully replicates the scientific manuscript published in the *Journal of Geophysics Research: Space Physics*, 129, e2024JA032601, https://doi.org/10.1029/2024JA032601. I contributed to the conceptualization of the study, the formal analysis, the software development, the validation, the visualization, and the writing of the manuscript. The manuscript was reviewed and edited by the co-authors: Dr. Sowmya Krishnamurthy, Dr. Nina-Elizabeth Nèmec, and Dr. Alexander I. Shapiro.

Keypoints

- We estimate the solar irradiance at any point in the ecliptic plane, accounting for the evolution of magnetic features on the solar surface, using area coverages obtained from the Surface Flux Transport Model.
- The method agrees for values in the ultraviolet but disagrees for the TSI when compared to the interpolation of Earth-based measurements.
- We calculate the correlation between our method and the phase shifting and the interpolation of Earth-based measurements of irradiance.

2.1 Abstract

The primary external energy input to planetary atmospheres comes from solar radiation. Accurate estimates of solar irradiance are needed in order to understand atmospheric conditions at other planets. Many studies have interpolated Earth-based irradiance measurements at other planets, disregarding the evolution of solar features, which are responsible for the irradiance variability. We present an approach for assessing solar irradiance at other planets by using synthetic full surface magnetograms of the Sun, generated by the Surface Flux Transport Model, and then converted into sunspots and faculae areas. Following the Spectral And Total Irradiance REconstruction approach, we compute the irradiance as the sum of contributions from sunspots, faculae, and the quiet Sun. We calculate the S-index, which is a proxy for near-ultraviolet irradiance, and the total solar irradiance, which is the wavelength-integrated value. We demonstrate that a simple phase shift of the Earth-observed total solar irradiance does not produce reliable estimates in the ecliptic. By comparing and correlating our results with the interpolated measurements, we find that the two models agree in the S-index variability, because faculae have a long lifetime, so the effect of the solar rotation becomes less important. Conversely, the methods disagree strongly in the total solar irradiance, since sunspots have a short lifetime, and the interpolation does not take into account their emergence and evolution on the far side of the Sun, as it only uses the information of the disc visible for an Earth-bound observer.

2.2 Introduction

Solar radiation is the main source of external energy input to planetary atmospheres, playing a crucial role in the atmospheric structure and composition. In particular, the ultraviolet (UV) irradiance drives the photochemistry of the Earth's middle atmosphere (Gray et al. 2010), while the extreme ultraviolet (EUV) radiation is responsible for the photochemistry of the upper atmospheres of the planets in the Solar System (Fox, Galand, and Johnson 2008). A number of general circulation models have been employed in order to understand the mechanisms that rule the atmospheric behavior. These models need, as an input, the values of solar irradiance entering the planetary atmosphere. However, the direct measurements of such irradiance are scarce, so that it must be obtained with modeling.

Several studies have used measurements made at Earth to evaluate the solar irradiance at other planets (e.g. Ramstad et al. 2015; Peter et al. 2014). These studies are based on the assumption that irradiance from the non-rotating Sun is constant and, thus, the only source of irradiance variability is the solar rotation (hereafter referred as the lighthouse approximation). Then, to obtain the irradiance entering the atmosphere of a planet, the measurements made from Earth are either phase-shifted (see Section 2.4.1) or interpolated (see Section 2.4.2) according to the relative position of the Earth and the planet and then scaled to the Sun-planet distance (Thiemann et al. 2017; Thiemann et al. 2021).

There have been efforts to test the accuracy of the lighthouse approximation in the literature. For example, Thiemann et al. (2021) used measurements from the Extreme Ultraviolet Monitor (EUVM, Eparvier et al. 2015) onboard the Mars Atmosphere and Volatile EvolutioN (MAVEN) spacecraft to conclude that the error introduced by the lighthouse approximation can be comparable to the amplitude of the solar rotational variability. Quémerais et al. (2019) developed an algorithm which combines measurements from the Solar Wind ANisotropies (SWAN) Solar Heliospheric Observatory (SOHO) Lyman-α photometer with Earth-based solar flux measurements to derive the irradiance at Lyman-α for any direction in the ecliptic plane. They have found that the SWAN-based method is superior to the interpolation at periods of high solar activity. On the contrary, the interpolation method works better than the SWAN-based method at periods of low solar activity.

The lighthouse approximation introduces an error that depends on the angle within the ecliptic plane between Earth and the planet of interest, centered on the Sun. This Earth-Sun-planet angle (ϕ) is shown in Figure 2.1. This error is a consequence of the constantly evolving distribution of magnetic fields on the solar surface. The magnetic fields emerge from the interior of the Sun, forming active regions on the surface, which evolve and decay on timescales from days to months (see e.g. Solanki, Krivova, and Haigh 2013 and references therein). In the absence of active regions, the solar irradiance is constant. In this case, the solar irradiance measured at Earth can be scaled to other positions in the Solar System with a simple function of distance. The active regions, however, make the solar surface heterogeneous and lead to anisotropic solar irradiance, as well as the temporal variability of the irradiance.

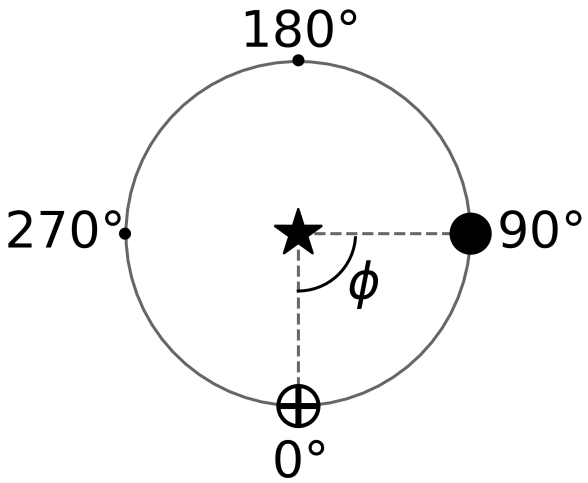

Figure 2.1: Earth-Sun-planet angle (ϕ), within the ecliptic plane. The Earth and the planet of interest are depicted by the symbols $\oplus$ and the full circle, respectively, and the star depicts the Sun. Solar rotation is anti-clockwise.

There are two main sources of solar variability on the timescales from days to months. The first is brought about by solar rotation: the active regions rotate in and out of view, similar to the behavior of a lighthouse. The second is attributed to the evolution of active regions. Nèmec et al. (2020) showed that the variability of the solar irradiance in the visible spectral domain is dominated by rotation for timescales between $4-5$ days and the synodic solar rotation period (27.3 days). For timescales shorter than $4-5$ days or longer than a solar rotation, the variability is dominated by the evolution and emergence pattern of magnetic features, which is not taken into consideration by the lighthouse approximation.

In this study, we develop a new method for estimating solar irradiance at different positions within the ecliptic plane of the Solar System, for the total solar irradiance (TSI, i.e., spectrally-integrated irradiance) and for the S-index (a proxy for near-ultraviolet). We take into consideration the evolution of active regions in the Sun and follow an approach rooted in the Spectral And Total Irradiance REconstruction model (SATIRE, Fligge, Solanki, and Unruh 2000; Krivova et al. 2003; Krivova, Solanki, and Unruh 2011). Our SATIRE-inspired approach is described in Section 2.3 and then compared to both simple shifting of irradiance measurements and the interpolation method in Section 2.4. The conclusions of this work are drawn in Section 2.5.

2.3 Methods

In order to calculate the TSI and the S-index, we combine spectra of the quiet Sun (i.e., regions on the solar surface free from any visible manifestations of magnetic activity) and the magnetic features with their corresponding area coverages on the visible solar disc. Each of these aspects will be covered in this section.

2.3.1 Spectral and total solar irradiance

The SATIRE-inspired approach makes use of the intensity of the quiet Sun and of magnetic features, weighted by their areas on the solar disc. It takes into account the distribution and time evolution of magnetic features on the full solar surface so that the irradiance variability in any given direction can be directly calculated. The approach is based on the assumption that solar irradiance variations on timescales longer than one day can be explained by variations in the surface magnetic fields (Fligge, Solanki, and Unruh 2000; Krivova et al. 2003).

The spectral solar irradiance (SSI) at the Earth-Sun-planet angle ϕ (see Figure 2.1), at an orbital inclination θ, for a certain time (t) and wavelength (λ) is computed as the sum of two components:

$$E^{\phi\theta}(t,\lambda) = E_{\mathrm{q}}(\lambda) + E_{\mathrm{a}}^{\phi\theta}(t,\lambda). \tag{2.1}$$

Then, the TSI is obtained by integrating the SSI calculated using Eq. 2.1 over all wavelengths.

In Eq. 2.1, $E_{\mathrm{q}}(\lambda)$ is the time-independent spectral irradiance from the quiet Sun. $E_{\mathrm{q}}(\lambda)$ does not depend on ϕ and θ, and is given by

$$E_{\mathrm{q}}(\lambda) = \sum_i I_{\mathrm{q}}(\lambda,\mu_i)\Delta\Omega_i, \tag{2.2}$$

where $I_{\rm q}(\lambda, \mu_i)$ is the intensity emerging from the quiet Sun for a given wavelength λ along the direction μ_i. The solar surface is divided into many pixels indexed with i (see Section 2.3.2) and $\Delta\Omega_i$ is the solid angle subtended by the i-th pixel as seen from the planet.

The term $E_{\rm a}^{\phi\theta}(t, \lambda)$ in Eq. 2.1 represents the contribution to the SSI from magnetic activity, and can be decomposed as

$$\begin{aligned} E_{\rm a}^{\phi\theta}(t, \lambda) = &\sum_i \alpha_{\rm u}^{i\phi\theta}(t)[I_{\rm u}(\lambda, \mu_i) - I_{\rm q}(\lambda, \mu_i)]\Delta\Omega_i \\ &+ \sum_i \alpha_{\rm p}^{i\phi\theta}(t)[I_{\rm p}(\lambda, \mu_i) - I_{\rm q}(\lambda, \mu_i)]\Delta\Omega_i \\ &+ \sum_i \alpha_{\rm f}^{i\phi\theta}(t)[I_{\rm f}(\lambda, \mu_i) - I_{\rm q}(\lambda, \mu_i)]\Delta\Omega_i. \end{aligned} \tag{2.3}$$

Here, $I(\lambda, \mu_i)$ are the intensities of the magnetic features, namely, sunspot umbrae (u), sunspot penumbrae (p), and faculae (f). Unruh, Solanki, and Fligge (1999) have shown that including only the quiet Sun, sunspots, and faculae in the computations is adequate to explain the observed SSI and TSI variations (see e.g. Solanki, Krivova, and Haigh 2013; Ermolli et al. 2013). We employ the intensities computed by Unruh, Solanki, and Fligge (1999) with the use of the ATLAS9 radiative transfer code (Kurucz 1992; Castelli and Kurucz 1994), under the assumption of local thermodynamic equilibrium (LTE).

The intensities are derived for 1221 wavelengths, ranging from 9.09 nm to 10020 nm, with varying spectral resolution, but only values computed above 160 nm can be trusted, due to the assumption of LTE in ATLAS9 (Tagirov et al. 2019). To account for the centre-to-limb variation of the intensity, the intensities are calculated for 11 positions on the solar disc corresponding to $\mu = 1.0$ (disc center), 0.9, 0.8, 0.7, 0.6, 0.5, 0.4, 0.3, 0.2, 0.1, and 0.05. For intermediate disc positions, i.e. when μ_i of the pixel is different from these 11 values, the intensities are interpolated to the value of μ_i.

In Eq. 2.3, $\alpha^{i\phi\theta}(t)$ are the fractional area coverages per pixel by a given magnetic feature. Depending on ϕ and θ, an observer sees different parts of the solar surface, i.e., the visible solar disc changes. The dependence of the SSI on the observer's location comes solely from $E_{\rm a}^{\phi\theta}(t, \lambda)$, because the disc area coverages of sunspots and faculae depend on ϕ and θ. Therefore, the calculation of the SSI for different ϕ and θ angles requires that the distribution of sunspots and faculae over the entire solar surface is known, in addition to their intensities.

In the following section, we describe the method used to obtain the area coverages of magnetic features that are needed to compute the SSI and TSI at various locations of the observer. Several studies have used this method to model solar irradiance at arbitrary inclinations (see e.g. Nèmec et al. 2020; Sowmya et al. 2021a). We note that for any ϕ and θ, an observer sees only half of the solar surface and therefore the summations in Eqs. 2.2 and 2.3 are carried out only over the pixels on the visible disc. Furthermore, to compare our results with those which use measurements made exclusively on Earth, we limit our analysis to the solar disc as observed from the ecliptic plane, and therefore the superscript θ will be omitted from now on.

2.3.2 Area coverages

We use the spots and faculae area coverage maps obtained by Nèmec et al. (2020), who utilised the Surface Flux Transport Model (SFTM) in the form of Cameron et al. (2010). We summarise their approach here briefly, but refer to Nèmec et al. (2020) for details.

In the SFTM, magnetic flux emerges as a bipolar magnetic region and, once emerged, the flux evolves due to advection, diffusion and large scale flows (i.e. the meridional flow and differential rotation). The emergence of the bipolar magnetic regions is based on the semi-empirical input record of sunspot groups, as described in Jiang et al. (2011), with the addition that the emergence longitude of the bipolar magnetic regions is randomised in order to get the full surface distribution of the regions, as needed for our purpose. We note that the statistical input record preserves the latitudes of emergence (i.e. the solar butterfly diagram), but due to the nature of the semi-empirical record, the actual sizes and emergence of the active regions cannot be directly compared on a day-to-day basis to the observed distribution on the Sun. While the record by Jiang et al. (2011) dates back to 1700, we only utilise the synthesized solar cycle 22, which represents a cycle of intermediate activity level.

Subsequently, the flux distribution is converted into spot and faculae areas. Following the input record, sunspots are immediately emerged at their largest size, i.e. we neglect the growing phase. On the day of emergence, Nèmec et al. (2020) calculated the size of the spots using the given areas in the input record, but needed to add a simple model to take into account the growth and decay of the spots. Penumbral area coverages are taken as 80 % of the spot areas, while the remaining 20 % is attributed to umbrae. Using the spatial and temporal distribution of spots, the magnetic flux in each pixel of the full surface map is corrected for the spot flux. The remaining magnetic field in the pixel is ascribed to faculae. The area coverages of faculae are determined following the saturation threshold approach of the SATIRE model (Fligge, Solanki, and Unruh 2000; Krivova et al. 2003). From the full surface maps of area coverages, the coverages on the visible disc for any ϕ can be computed by making appropriate geometrical transformations (see e.g. Sowmya et al. 2021b).

Figure 2.2 illustrates an example of the synthetic distribution of magnetic features on the full solar surface and the visible discs corresponding to ϕ angles of 0°, 90°, 180°, and 270°. The spatial distribution as well as the area coverages of spots and faculae on the visible disc are very different depending on ϕ, as clearly shown by the orthographic projections in Figure 2.2.

2.3.3 S-index

The Mg II spectral lines around 280 nm exhibit one of the largest solar irradiance variability in the near-UV. Due to this, the Mg II index (core to wing ratio) is used as a proxy for the irradiance variability in the UV and EUV regime. The Mg II index is also shown to be a better proxy for solar EUV than the widely used F10.7 index (Viereck et al. 2001). Very accurate and high resolution spectra of the Mg II lines synthesized in non-LTE as a function of μ are needed to correctly determine the Mg II index and its dependence on ϕ. Since such detailed modeling is currently unavailable and beyond the scope of this work, we instead use the Ca II H and K lines to investigate the irradiance changes in the near-UV. Such a choice is directly driven by the strong linear correlation between the irradiance in the Mg II and Ca II lines (DeLand and Marchenko 2013).

We quantify the variability in Ca II via the well-known chromospheric activity indicator, namely the S-index (Vaughan, Preston, and Wilson 1978). The S-index is calculated as the ratio of the summed fluxes in the Ca II H and K line cores to the summed fluxes in two spectral regions near the blue wing of the K line and the red wing of the H line. This index was established by the Mt. Wilson Observatory, and has been recorded for lower main-sequence stars since 1966 (Wilson 1978).

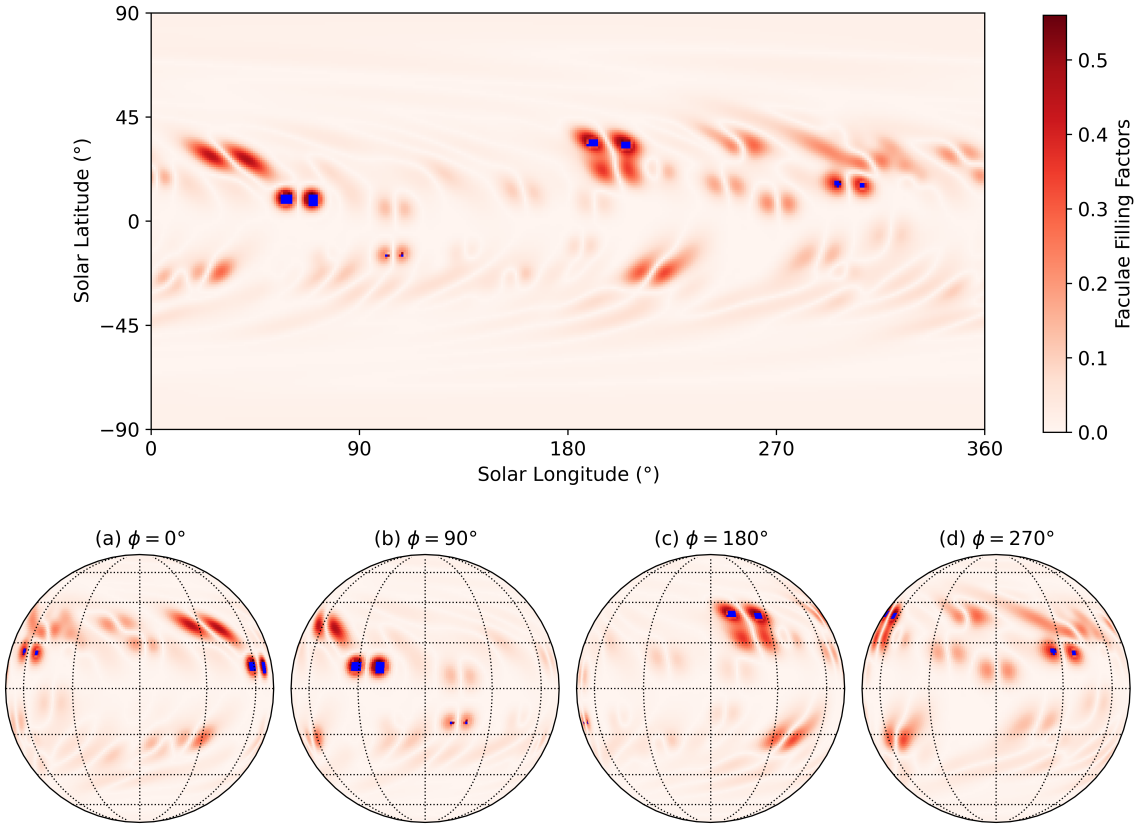

Figure 2.2: Snapshot of a synthetic distribution of faculae (red shades) and sunspots (blue pixels). Top: full surface map. Bottom: orthographic projections centered at the ϕ angle indicated above each panel. An observer placed at $\phi = 0°$ views the visible solar disc as in panel (a), for example.

The formation of Ca II H and K lines spans a wide range of heights in the solar atmosphere. The line cores are formed in the chromosphere, above the solar photosphere, where LTE assumptions are no longer valid. Sowmya et al. (2021a) followed a non-LTE approach to compute the emergent intensities of the quiet Sun and faculae, using the RH code (Uitenbroek 2001). Here, again, the intensities are computed for different disc position, as explained in Section 2.3.1, in order to account for center-to-limb variations.

We use the spectra from Sowmya et al. (2021a) in Eqs. 2.2 and 2.3 to determine the near-UV SSI variability, neglecting the contribution from spots, since the variability in the Ca II H and K lines are mainly driven by faculae, as shown by Sowmya et al. (2021a) and Sowmya et al. (2023). The S-index is then obtained according to Equation 1 of Sowmya et al. (2021a).

2.4 Results and discussion

The synthetic calculations of TSI and S-index in this work are performed for two one-year periods within solar cycle 22, using the methods presented in Sections 2.3.1 and 2.3.3. The first year is a period of high solar activity and it is centered on the day with the maximum disc area coverage of faculae during the cycle. The second is a period of low solar activity and comprises the last 365 days of solar cycle 22. Figure 2.3 shows the obtained TSI for the whole solar cycle 22, as well as the chosen periods of high and low solar activity.

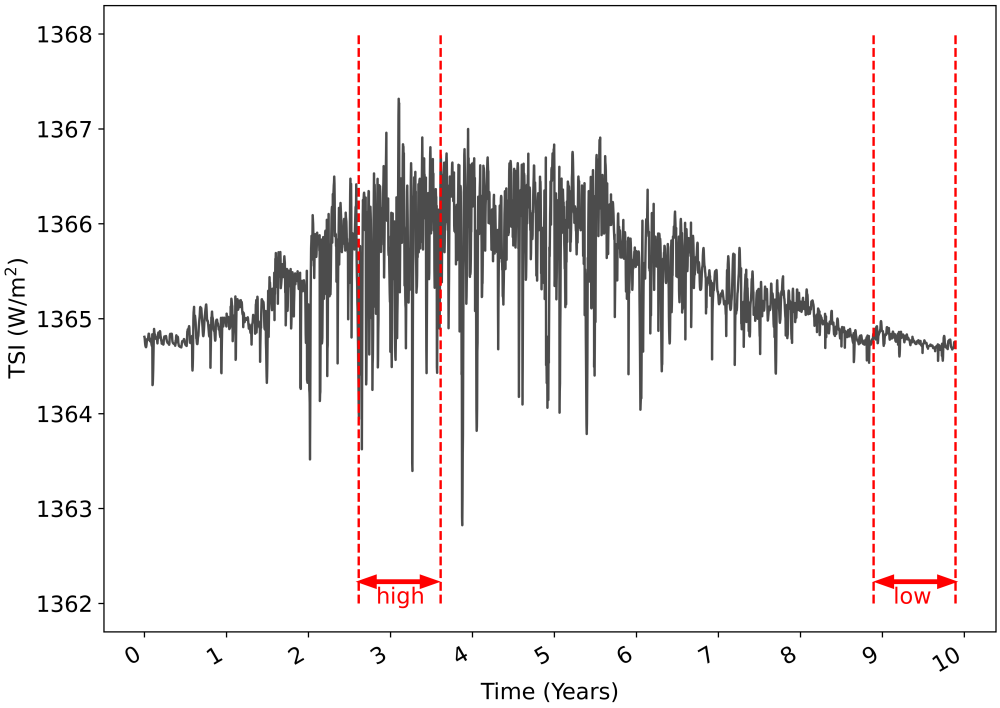

Figure 2.3: Synthetic TSI based on the magnetic flux of the visible disc for solar cycle 22. The one-year time periods of high and low solar activity used in this work are marked by red dashed lines.

We define the normalized variability on the time scale of a solar rotation as

$$\Delta E^{\phi}(t,\lambda) = \frac{E^{\phi}(t,\lambda) - \langle E^{\phi}(t,\lambda)\rangle_{81}}{\langle E^{\phi}(t,\lambda)\rangle_{81}}, \tag{2.4}$$

where $\langle E^{\phi}(t,\lambda)\rangle_{81}$ is the moving average with an 81-days time window centered on t. We choose the time window of 81-days, which is the equivalent to three solar rotations, in order to remove the effects that arise due to the transit of the magnetic features.

For the S-index, we simply calculate the rotational variability as

$$\Delta S^{\phi}(t) = S^{\phi}(t) - \langle S^{\phi}(t)\rangle_{81}, \tag{2.5}$$

where $S^{\phi}(t)$ is the S-index at time t and angle ϕ, and $\langle S^{\phi}(t)\rangle_{81}$ is the 81-days moving average.

2.4.1 Phase shifts and cross-correlation analysis

In the phase shift approach, the irradiance at the planet of interest is obtained by simply phase shifting the irradiance measurements made at Earth and scaling them to the Sun-planet distance. In this approach, we neglect the evolution of active regions and assume that in the absence of solar rotation, the solar irradiance is constant.

Here, we perform an experiment to assess the accuracy of the phase shift approach at three different ϕ angles in the plane of the solar equator: $90°, 180°$, and $270°$ (see Figure 2.1). According to the phase shift approach, the irradiance values at these angles are

$$E^{90^\circ}(t, \lambda) = E^{0^\circ}(t - 7\ d, \lambda) \tag{2.6}$$

$$E^{180^\circ}(t, \lambda) = E^{0^\circ}(t - 14\ d, \lambda) \tag{2.7}$$

$$E^{270^\circ}(t, \lambda) = E^{0^\circ}(t - 21\ d, \lambda), \tag{2.8}$$

with t in days (d). The time periods are equivalent to the angular distance, assuming the synodic solar rotation to be ~ 28 days. The irradiance at $\phi = 90°$ is expected to be the irradiance at $\phi = 0°$ a quarter of a solar rotation (seven days) earlier, and so on for the other ϕ angles.

Figure 2.4 shows the comparison between TSI values calculated with the phase shift approach (i.e. with Eqs. 2.6–2.8, see blue, green, and red curves) and with the SATIRE-based approach (i.e. with Eqs. 2.1–2.3, see black curves). The comparison is given for periods of high (left panels) and low (right panels) solar activity during solar cycle 22. We note that the dips in the time series are indicative of spot transits. Since the spots are dark, they reduce the TSI. On the contrary, the peaks are caused by faculae, which are bright regions that increase the TSI.

The variability of the S-index computed with the phase shift and with SATIRE-based approaches is shown in Figure 2.5, following the same color scheme as in Figure 2.4. We note that the S-index calculations are performed by neglecting spots, since Sowmya et al. (2023) showed that the solar S-index and its variability are mainly driven by faculae. Hence, the variability seen in Figure 2.5 are attributed to faculae. The solar rotational cycles are clearly visible in the time series at both high and low activity periods.

In Table 2.1, we show the linear Pearson correlation coefficients obtained for each of the cases presented in Figures 2.4 and 2.5. The correlation between the reference and the shifted TSI time series is poor during both periods of solar activity. In addition, the correlation worsens with increasing ϕ. This can be attributed to spots which dominate TSI at shorter timescales. The spots are short-lived and evolve quickly on the solar surface. Because of that, the visible disc at various ϕ differs considerably and the correlation becomes low when a shift of the order of a few days is applied. This suggests that a simple phase shift of the irradiance time series is not a good solution for determining the TSI and its variability at different positions within the Solar System ecliptic plane.

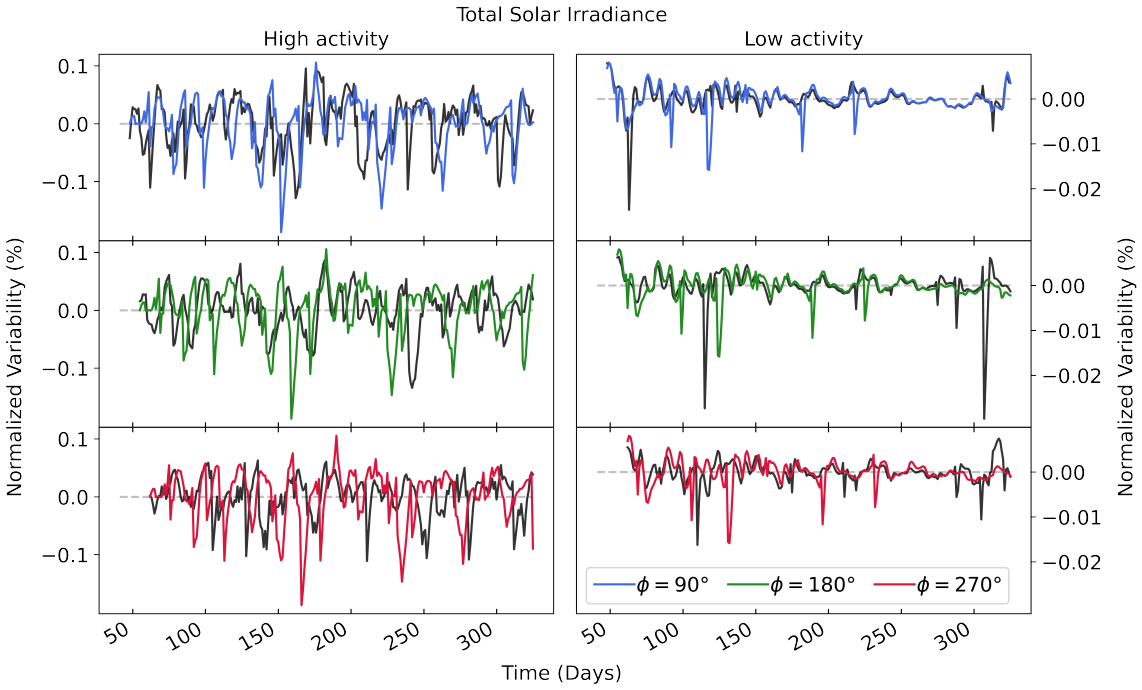

Figure 2.4: Synthetic time series of the normalized TSI variability for periods of high (left) and low (right) solar activity. The panels show the calculated (black) and phase shifted (colors) variability. From top to bottom, the panels show $\phi = 90°$ (blue), $\phi = 180°$ (green), and $\phi = 270°$ (red).

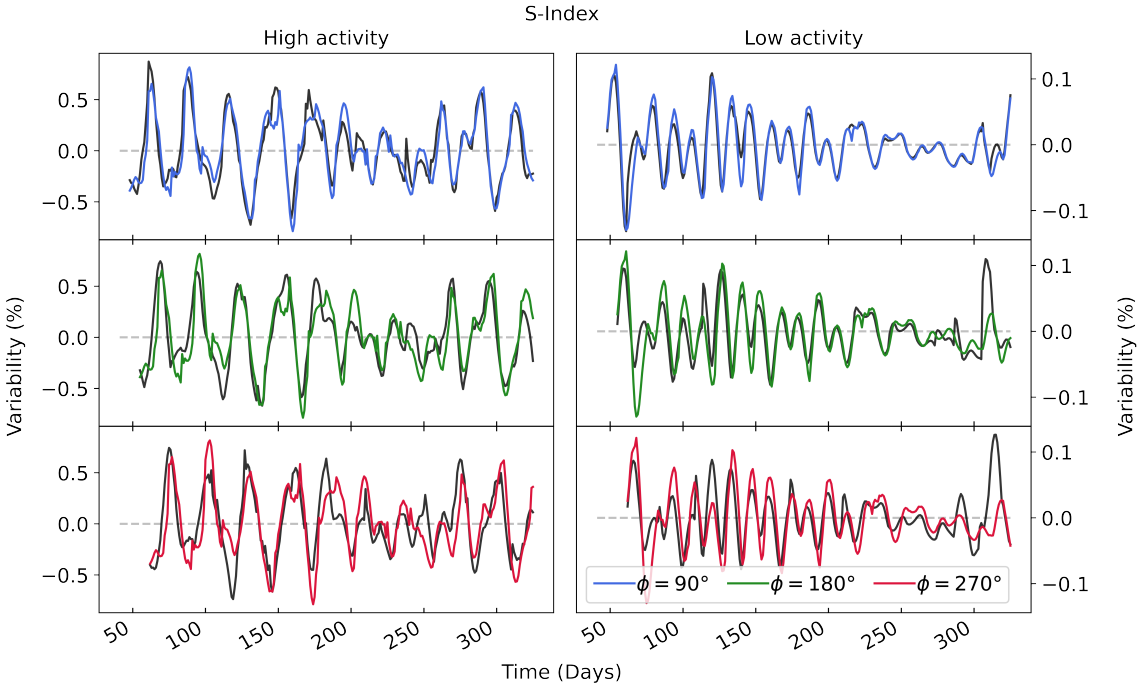

Figure 2.5: The same as in Figure 2.4, but for the S-index variability.

Table 2.1: *Correlation Coefficients Between the Calculated and the Phase Shifted Time Series of Irradiance.*

	High activity		Low activity	
ϕ	TSI	S-index	TSI	S-index
90°	0.39	0.92	0.47	0.93
180°	0.10	0.84	0.17	0.75
270°	−0.10	0.75	0.18	0.63

The S-index curves at $\phi = 0°$ and at $\phi = 90°$ shifted by seven days (blue curves) show a very good correlation, with linear correlation coefficients above 0.9. The difference between these two time series at $\phi = 90°$ and the series at $\phi = 0°$ arises from the evolution of faculae over the course of seven days. Since the faculae survive on the solar surface longer than most spots, the time series recorded seven days apart still sees most of the original faculae features and thus the correlation between the time series is high. With increasing ϕ, the correlation between the time series generally decreases, although the correspondence is still reasonably high. This indicates that shifting the solar irradiance time series measured at Earth to other positions within the ecliptic plane works relatively better for S-index than for TSI.

We also determine the cross-correlation between the time series. With this analysis, our aim is to find how many days (forward or backward) the irradiance time series at $\phi = 90°, 180°$, and 270° should be shifted in order to achieve the highest correlation coefficient, r, to the time series at $\phi = 0°$. This is done by shifting the time series day by day, with a time window ranging from a solar rotation in the past to a solar rotation in the future, and comparing them with the time series at $\phi = 0°$. Table 2.2 shows the results of the cross-correlation analysis. Negative shifts indicate preceding days (the same logic as in Eqs. 2.6–2.8), while positive shifts indicate following days.

Table 2.2: *Results of the Cross-Correlation Analysis Between the Time Series.*

	High activity				Low activity			
	TSI		S-index		TSI		S-index	
ϕ	Shift (days)	r	Shift (days)	r	Shift (days)	r	Shift (days)	r
90°	−6	0.45	−6	0.92	−7	0.47	−6	0.94
180°	−22	0.19	−13	0.87	−5	0.30	+13	0.82
270°	+4	0.38	+7	0.90	+7	0.41	+7	0.88

Note. Given are the maximum correlation coefficients (r) and their corresponding shifts with respect to the time series at $\phi = 0°$. Negative shifts indicate preceding days, while positive shifts indicate following days.

As discussed previously, an angular distance of $\phi = 90°$ should correspond approximately to -7 days, $\phi = 180°$ to -14 days, and $\phi = 270°$ to -21 days. The cross-correlation analysis gives the expected result for $\phi = 90°$, even though the coefficients are relatively low for the TSI. For higher ϕ angles, the maximum correlation coefficients for the TSI do not seem to have any physical meaning, since the shifts are very distant from what is expected. As for the S-index, some of the maximum coefficients are achieved when the time series are shifted one entire solar rotation ahead of what is expected (positive shifts). From Figures 2.4 and 2.5 and Tables 2.1 and 2.2, we infer that a simple phase shift is not sufficient to provide good correlation results and, accordingly, irradiance estimates.

2.4.2 Comparison with interpolated Earth-based measurements

As described by Thiemann et al. (2017), the interpolation method estimates the irradiance at a certain planet (or angle ϕ within the ecliptic plane) for a day t_d, by using measurements at Earth ($E_\oplus$) made before ($t_d - \Delta t_1$) and after ($t_d + \Delta t_2$) the visible solar disc rotates past the planet. The time differences Δt_1 and Δt_2 follow the same logic as in Eqs. 2.6 to 2.8. For example, if the Earth-Sun-planet angle ϕ is 90° today, the irradiance at the planet would be estimated as the weighted sum of the irradiance at Earth ∼7 days ago and ∼21 days in the future. The interpolation is given by

$$E(t_d, \phi) = \frac{w_1 \; E_\oplus(t_d - \Delta t_1) + w_2 \; E_\oplus(t_d + \Delta t_2)}{r^2(t_d)}, \tag{2.9}$$

where $r^2(t_d)$ is the distance between Earth and the planet on day t_d, in AU. The measurements are linearly interpolated and weighted, and the weights w_1 and w_2 are proportional to the periods Δt_1 and Δt_2. In the example given, the weights w_1 and w_2 would be 0.75 and 0.25, respectively. For a more detailed explanation of the method, see Section 2.1 from Thiemann et al. (2017).

We apply the interpolation method to the irradiance time series at $\phi = 0°$, and determine the irradiance at $\phi = 90°, 180°$, and 270°. Then, we compare these interpolated time series to the ones evaluated at $\phi = 90°, 180°$, and 270° using our SATIRE-inspired approach, by considering the Pearson correlation coefficient of the time series at each ϕ. The coefficients are shown in Table 2.3. Figure 2.6 shows such a comparison for the TSI during periods of high and low activity. The time series calculated using our SATIRE-inspired approach at ϕ (black curves) and the values interpolated from $\phi = 0°$ to $\phi = 90°, 180°$, and 270° (in colors) differ greatly.

Table 2.3: *Correlation Coefficients Between the Calculated and the Interpolated Time Series of Irradiance.*

	High activity		Low activity	
ϕ	TSI	S-index	TSI	S-index
90°	0.30	0.93	0.49	0.93
180°	0.17	0.93	0.21	0.87
270°	0.24	0.93	0.45	0.90

The interpolation method misses the exact timing of most spot transits (valleys), especially for periods of high solar activity. During periods of low solar activity, extrapolating the data seems to overestimate the duration and/or intensity of the sunspots. For all three positions around the Sun, the correlation between the calculated and the interpolated TSI variability does not surpass 0.49. This suggests further that the interpolation of the TSI variability observed at Earth to other planets does not represent the true variability seen at those planets. By comparing Figures 2.4 and 2.6, however, the valleys and peaks characteristics of each time series are better reconstructed with the interpolation than with the phase shifting method.

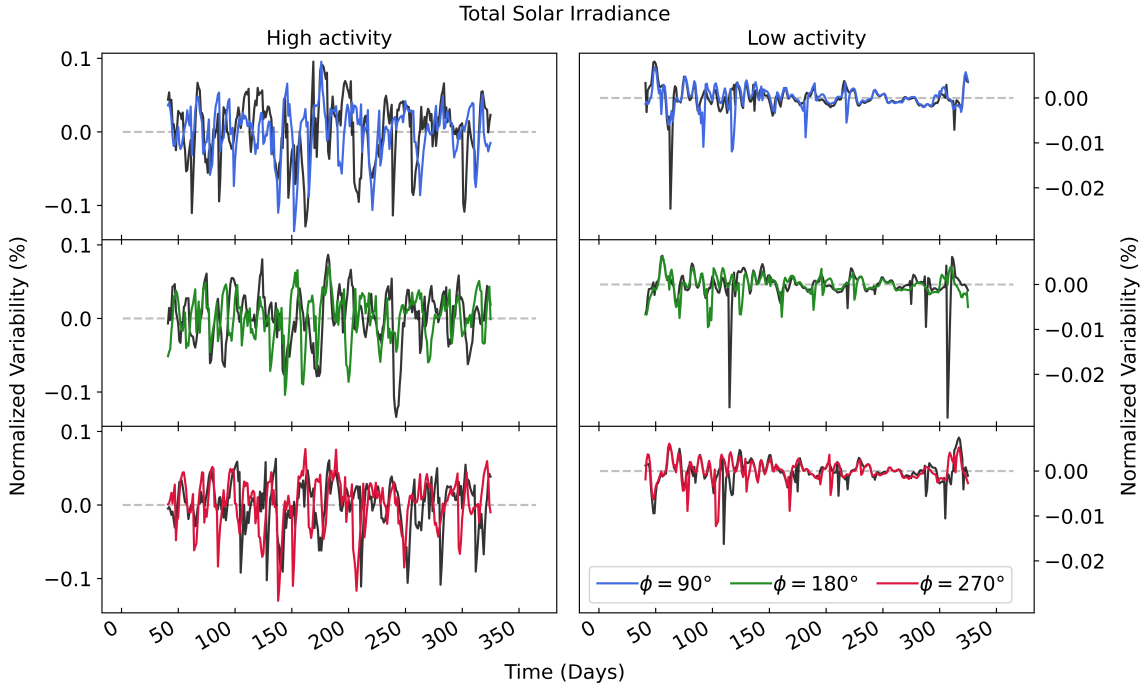

Figure 2.6: Synthetic time series of the normalized TSI variability for periods of high (left) and low (right) solar activity. The panels show the variability calculated using our SATIRE-inspired approach (black) and the interpolation method (colors). From top to bottom, the panels show $\phi = 90°$ (blue), $\phi = 180°$ (green), and $\phi = 270°$ (red).

Following the same scheme, Figure 2.7 shows the time series of the S-index variability at high and low activity periods. Contrary to the TSI case, the correlations between the calculated and interpolated S-index variability are high, and the curves look very similar. Again, the shapes of the interpolated irradiance time series are more in agreement to the ones obtained with the SATIRE-inspired approach than the ones estimated with the phase shifting method (Figure 2.5).

On one hand, the interpolation method works very well for the proxy of UV wavelengths because facular regions evolve very slowly, so that the evolution variability they induce is not significant on solar rotation timescales. On the other hand, the application of the interpolation method for the TSI or wavelengths which are dominated by sunspots would result in a very large error in the estimated irradiance.

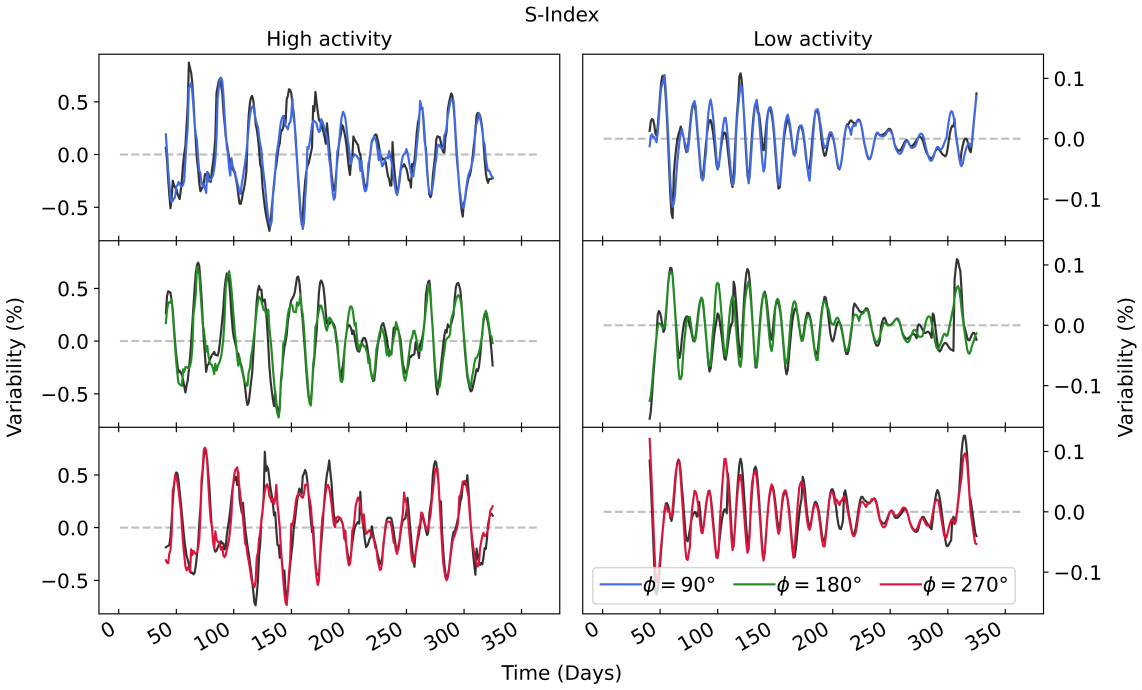

Figure 2.7: The same as in Figure 2.6, but for the S-index variability.

2.5 Summary and conclusions

In this study, we present a method for estimating solar irradiance within the ecliptic plane. First, we use a synthetic statistical model of magnetic field transport, as well as semi-empirical information on active regions sources in order to build a synthetic model of faculae and spots area coverages observed at any position within the ecliptic plane during solar cycle 22. Then, we compute synthetic values of spectral solar irradiance at several Earth-Sun-planet angles in the Solar System using a method that is built on the SATIRE model for solar irradiance variability reconstruction.

Using our SATIRE-inspired synthetic model, we evaluate the TSI and the S-index - which is a proxy for irradiance at near-UV wavelengths, at four Earth-Sun-planet angles: $\phi = 0°, 90°, 180°$, and $270°$, for a year of high solar activity and a year of low solar activity. We apply a simple phase shift to the time series at $\phi = 90°, 180°$, and $270°$, proportional to the solar rotation, and compare the results with the time series at $\phi = 0°$. We conclude that a simple phase shift of the data is not enough to obtain good estimates of solar irradiance.

We also compared our method with the traditional interpolation method (Thiemann et al. 2017). This method consists of a "lighthouse" model, where Earth-based measurements of SSI are interpolated to other planets assuming that irradiance variability is only caused by solar rotation.

We investigate the correlation of the time series computed with our SATIRE-inspired approach and the interpolated time series. The results show that there is a high correlation between the interpolation and the SATIRE-inspired approach when it comes to the S-index. Due to the relatively greater lifetime of faculae, which are the sources of solar UV variability, the interpolation method is able to catch slow changes in irradiance. However, the correlation drops significantly for the TSI, since it is dominated by sunspots, which emerge, evolve, and decay very fast. In this case, the interpolation method cannot properly account for the effect of spots, which are relatively short-lived and do not survive a full solar rotation. The SATIRE-inspired approach directly calculates the TSI, accounting for effects of faculae and spots, which is advantageous compared to the interpolation method.

We point out that our SATIRE-inspired approach for evaluating irradiance is still based on a synthetic model of full surface solar magnetograms and we used statistically valid emergences of magnetic regions to calculate the irradiance, and not real data. Therefore, the model is not capable of producing a nowcast estimation of solar irradiance. In the future, we will use information of far side helioseismology to derive the actual area coverages of magnetic regions.

Open Research Section

The area coverages data and flux intensities used for the calculations of irradiance in the study are available in De Oliveira (2024).

Acknowledgements

I. de O. would like to thank Laurent Gizon and Dan Yang for their contribution on reviewing the draft of this paper. This work was supported by the International Max Planck Research School for Solar System Science at the University of Göttingen.

Chapter 3

Estimation of spectral solar irradiance variability using low resolution magnetograms and seismic far side images

3.1 Motivation

In Chapter 2, I demonstrated how to estimate solar irradiance variability at various positions in the Solar System by using the area coverage of sunspots and faculae. Additionally, I compared the results to those obtained through the traditional interpolation method. The area coverages in that chapter were derived from synthetic full surface magnetograms, as detailed in Section 2.3.2.

For reconstructing solar irradiance variability at Earth, high-resolution magnetograms and continuum intensity images are available. The SATIRE-S model has demonstrated that this information is sufficient to accurately reconstruct irradiance variability. However, estimating irradiance variability at different positions in the Solar System requires data from the far side of the Sun, where neither continuum intensity images nor high-resolution magnetograms are available.

The main goal of this chapter is to determine whether we can still adequately reconstruct solar irradiance variability with limited resources, i.e., using only magnetic field data. To address this, I conduct a series of experiments, starting with the data used in the SATIRE-S model and progressively simplifying it to match the level of data available from the far side of the Sun. I employ an alternative approach to calculating area coverages using only magnetic field data. Through this method, I aim to estimate the SSI at different positions in the ecliptic plane using low-resolution magnetograms derived from seismic far side images. This approach is based on the assumption that the magnetic field can serve as a reliable proxy for the area coverage of sunspots and faculae to a sufficient extent.

3.2 Data

In this chapter, I use magnetic field data directly measured from the near side of the Sun, as well as data derived from helioseismic far side images. Additionally, I employ the SATIRE-S model and measurements of solar EUV obtained at Mars to validate the SSI variability results obtained with the proposed method for both the near and far sides of the Sun. The four datasets are described in the following sections.

3.2.1 Far side magnetic field maps from the FARM model

Helioseismic far side imaging, first introduced by Lindsey and Braun (2000), is a technique that utilizes seismic waves to monitor magnetic activity on the far side of the Sun. A study by Yang et al. (2024, in preparation) introduces the Far side Active Region Model (FARM), an innovative approach that uses improved seismic far side maps (Yang, Gizon, and Barucq 2023) and an empirical relationship to convert active region signals on the far side of the Sun into magnetic fields.

The Surface Flux Transport Model (SFTM, Baumann 2005), summarized in Section 2.3.2, is a an advective-diffusive model that describes the passive transport of the radial magnetic fields on the surface of the Sun, accounting for the effects of large-scale surface flows. In the traditional SFTM, new magnetic fields sources emerge only on the near side of the Sun.

Combining SFTM with FARM allows for modeling active regions on the far side of the Sun. The FARM model updates the SFTM with far side active regions on a daily basis, thus creating a dynamic and comprehensive model of the solar magnetic field. The output of the SFTM + FARM models – hereafter referred to simply as FARM – has a resolution of 360×180 pixels, with each pixel representing a latitude and longitude on the solar surface.

In this work, I use FARM magnetograms in order to estimate the area coverages of sunspots and faculae, and consequently the SSI, on any position within the ecliptic plane.

3.2.2 Near side magnetograms from SDO/HMI

The Helioseismic and Magnetic Imager (HMI, Schou et al. 2012) onboard the Solar Dynamics Observatory (SDO, Pesnell, Thompson, and Chamberlin 2012) observes the solar disc at the Fe I 6173 Å absorption line with a spatial resolution of 0.5 arcsecond per pixel. HMI produces full disc images, covering the entire near side solar disc, with a resolution of 4096×4096 pixels.

One key data product from HMI is the line-of-sight (LOS) magnetic field, measured at a cadence of 45 or 720 seconds. The LOS magnetic field represents the component directed towards the observer. These magnetograms are publicly available from the Joint Science Operations Center database[1], covering the period from May 2010 to the present. In Germany, all data from the SDO mission are managed, maintained, archived, and processed at the German Data Center for SDO[2], funded by the German Aerospace Center.

For this work, I use LOS magnetograms from the year 2015, a period of relatively strong solar activity near the peak of solar cycle 24. The magnetograms are obtained at a cadence of one per day, approximately at 10:00:00 UT, for a total of 365 days starting January 1st, 2015.

[1] http://jsoc.stanford.edu/HMI/Magnetograms.html
[2] https://www2.mps.mpg.de/projects/seismo/GDC-SDO/index.htm

In order to compare HMI magnetograms with FARM magnetograms, I first downsample the HMI magnetograms to 256×256 pixels – which is a similar resolution as the FARM magnetograms – using a linear interpolation function. This step is done to ensure that the data from both sources are compatible for analysis. In Section 3.4.2, I discuss the impact of the downsample on the results.

3.2.3 Extreme ultraviolet irradiance from MAVEN/EUVM

The Extreme Ultraviolet Monitor (EUVM, Eparvier et al. 2015) onboard the Mars Atmosphere and Volatile EvolutioN (MAVEN, Jakosky et al. 2015) spacecraft has been measuring the solar soft X-rays and EUV irradiance from Mars since October, 2014. This instrument measures the solar irradiance in three wavelength bands crucial for ionization, dissociation, and heating of Mars' upper atmosphere: 0.1 to 7 nm, 17 to 22 nm, and 121 to 122 nm. The data is collected at a 1-second cadence.

To generate a complete EUV spectrum at Mars, EUVM measurements are combined with time-interpolated observations of solar spectral emissions at Earth. This spectral irradiance model provides the EUV spectrum in the range of 1 to 190 nm with a resolution of 1 nm. The model outputs are available at a 1-minute cadence and as daily averages.

The EUVM data, along with the spectral irradiance model outputs, are publicly available at the MAVEN Science Data Center website[3].

3.2.4 Solar spectral irradiance from the SATIRE-S model

In this chapter, I compare the obtained SSI variability at the near side of the Sun to the Spectral And Total Irradiance REconstruction model for the Satellite era (SATIRE-S, Yeo et al. 2014). It uses intensity spectra of solar surface features derived by Unruh, Solanki, and Fligge (1999) with the radiative transfer code ATLAS9 (Kurucz 1992), which assumes local thermodynamic equilibrium (LTE).

Currently, the SATIRE-S is the most precise version of the SATIRE model. It uses full disc magnetograms and continuum intensity images of the Sun to estimate the area coverages of sunspots and faculae, which are then combined with their respective calculated intensity spectra in order to estimate the SSI and TSI.

The reconstructed SSI from SATIRE-S is available for the period from 1974 to the present and encompasses the solar spectrum in the wavelength range of 115 to 160 000 nm. The model is available for download at the website of the Max Planck Institute for Solar System Research[4].

[3] https://lasp.colorado.edu/maven/sdc/public/pages/datasets/euv.html
[4] https://www2.mps.mpg.de/projects/sun-climate/data.html

3.3 Method: From magnetic fields to area coverages

The original SATIRE model (Fligge, Solanki, and Unruh 2000; Krivova et al. 2003) uses full disc magnetograms and continuum intensity images in order to estimate the area coverage of sunspots and faculae. Sunspots are taken as regions of intense magnetic fields which are also dark in the continuum intensity images, while faculae are regions of intense magnetic field which are not already considered spots. Then, pixels with spots always have a spot filling factor of 1, while pixels with faculae have a varying facula filling factor, depending on the magnetic field strength, which increases linearly until reaching unity at a certain saturation value B_{sat}.

Since the only dataset available for all positions of the Solar System is the FARM magnetograms, I employ a simplified method to estimate the area coverages of sunspots and faculae in the i-th pixel of a magnetogram using only the radial magnetic field strength ($|B_i|$) in the pixel. This method was introduced by Nèmec et al. (2023) and it is described below.

While the estimation of faculae area coverage is similar to the original SATIRE method, the estimation of sunspots area coverage is different. In this method, the area coverage of sunspots is calculated for all pixels with magnetic field strength above a certain threshold B_{min}. Equations 3.1 and 3.2 give the area coverages of sunspots (α_s^i) and faculae (α_f^i), respectively:

$$\alpha_s^i = \begin{cases} 0 & \text{for} \quad |B_i| < B_{min} \\ \frac{|B_i| - B_{min}}{B_{max} - B_{min}} & \text{for} \quad B_{min} \leq |B_i| < B_{max} \\ 1 & \text{for} \quad |B_i| \geq B_{max} \end{cases} \tag{3.1}$$

$$\alpha_f^i = \begin{cases} 0 & \text{for} \quad \alpha_s^i > 0 \\ \frac{|B_i|}{B_{sat}} & \text{for} \quad |B_i| < B_{sat} \\ 1 & \text{for} \quad |B_i| \geq B_{sat} \end{cases} \tag{3.2}$$

In the Equations, B_{min} and B_{max} are the lower cut-off and upper saturation threshold for the magnetic field strength of sunspots, and B_{sat} is the saturation threshold for the magnetic field strength of faculae. The area coverage of sunspots is then divided in two parts: the area coverage of the umbrae ($\alpha_u^i = 0.2 \times \alpha_s^i$) and of the penumbrae ($\alpha_p^i = 0.8 \times \alpha_s^i$). The area coverages are then used in Equation 2.1 to calculate the SSI at a certain wavelength.

There are two important aspects to notice in the calculation of the area coverage of faculae from Equation 3.2. First, the area coverage of faculae is calculated *only* for pixels without sunspots, meaning that both features cannot co-exist in the same pixel, and that all values of magnetic field above B_{min} are considered spots, even though B_{sat} can be larger than B_{min}. Second, the area coverage of faculae is calculated for *all* pixels without sunspots, which means it also includes the quiet Sun – in contrast to the original SATIRE approach, where a region of noise around the quiet Sun would not be considered a magnetic feature at all. However, since the magnetic field strength of the quiet Sun is very low, the area coverage of faculae in these pixels is also very low, and the contribution of the faculae becomes negligible in the time scale of a solar rotation, which is the time scale of interest in this work.

In order to use this method in HMI LOS magnetograms, I transform the magnetic field in each pixel into the approximate radial magnetic field component by dividing the value in the pixel by the cosine of the heliocentric angle at that pixel, as discussed by Leka, Barnes, and Wagner (2017).

Figure 3.1 shows two examples of the area coverage of sunspots and faculae obtained with two parameter sets, compared to the respective HMI magnetogram (a) and continuum intensity image (b, showed as a reference for the ground truth of spots). The area coverages of c and d are obtained using the parameter values $B_{min} = 700$ G, $B_{max} = 1100$ G, and $B_{sat} = 500$ G, while the area coverages of e and f are obtained using the lower parameter values $B_{min} = 300$ G, $B_{max} = 700$ G, and $B_{sat} = 500$ G. Notice how the spots coverage in d looks more similar to the continuum intensity image than in f, which is due to the larger cut-off values of the magnetic field strength in the former case. In fact, the spots coverage shown in f is unrealistic, as it estimates sunspots where there are none, when compared to the image in b. Additionally, even though the faculae saturation threshold is the same in both cases, the faculae coverage in c is larger than in e, which is due to the different lower cut-off values of the magnetic field strength.

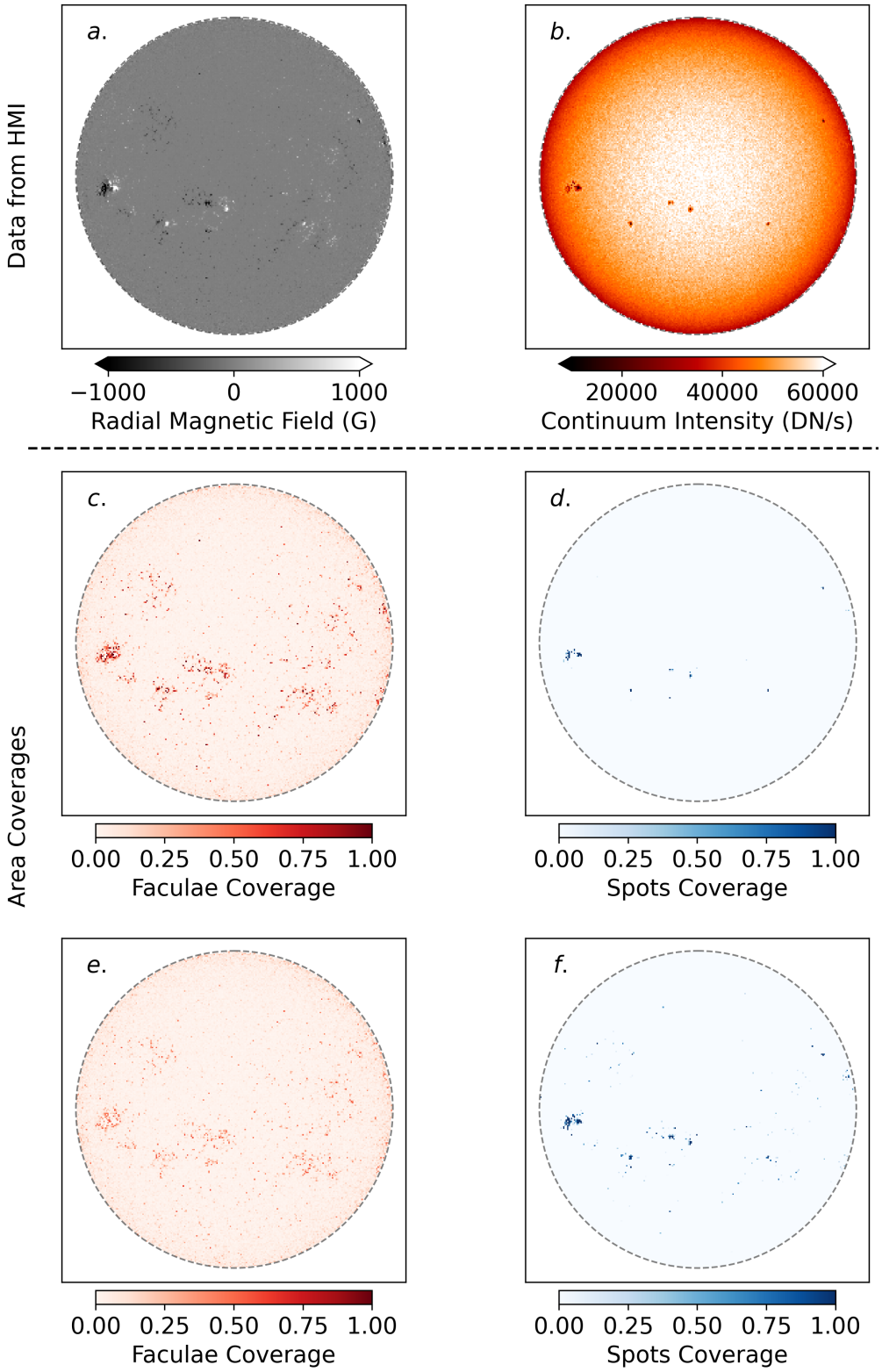

Figure 3.1: Near side solar disc at January 1st, 2015. **a)** HMI magnetogram. **b)** HMI continuum intensity. **c)** Area coverage of faculae and **d)** spots for $B_{min} = 700$ G, $B_{max} = 1100$ G, and $B_{sat} = 500$ G. **e)** Area coverage of faculae and **f)** spots for $B_{min} = 300$ G, $B_{max} = 700$ G, and $B_{sat} = 500$ G.

3.4 Estimating SSI variability using near side magnetograms

The primary objective here is to evaluate whether it is possible to accurately reconstruct irradiance variability using only magnetic field data. To achieve this, I compare the irradiance variability derived from the SATIRE-S model, considered the reference model, with the variability calculated from the area coverage of sunspots and faculae obtained from the near side HMI magnetograms. Identifying the optimal parameter values for calculating the area coverage is essential to ensure accurate results.

The methodology for calculating SSI variability in this section follows the same procedure outlined in Chapter 2 (Equations 2.1 to 2.4), as applied to an observer on Earth. The moving average in Equation 2.4 is calculated with a time-window of 81 days, consistent with the approach used in Chapter 2.

In this analysis, I present the SSI normalized variability (NV) for wavelengths of 200 nm and 700 nm, corresponding to the UV and VIS ranges, respectively. Figure 3.2 illustrates a strong linear correlation between the SSI NV at 200 nm and the S-index, which is used as a proxy for UV variability (see Section 2.3.3). This indicates that the variability at 200 nm is primarily influenced by faculae, similar to the S-index (Sowmya et al. 2023). In contrast, the SSI variability at 700 nm (in the red range) is predominantly driven by sunspots. By analyzing these two wavelengths, I can examine the contributions of both sunspots and faculae to the SSI variability.

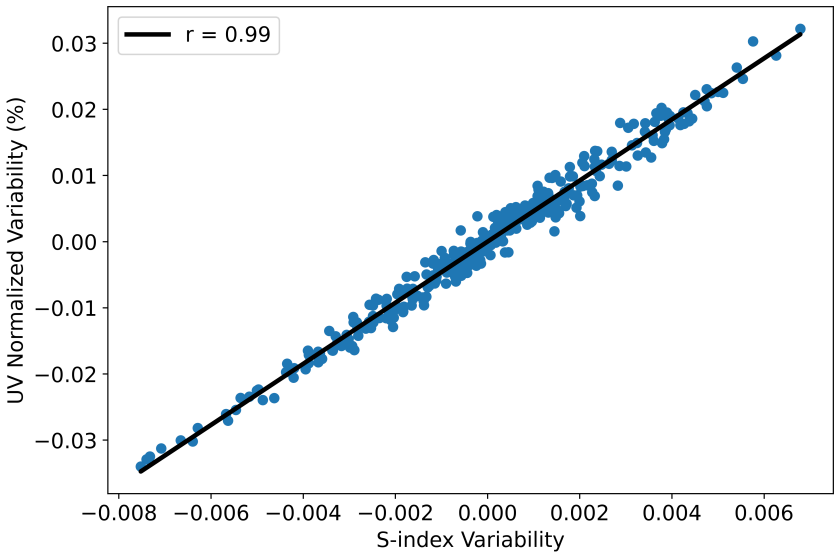

Figure 3.2: Correlation between the SSI normalized variability at 200 nm and the S-index variability determined from a time series of one year. The correlation coefficient between the curves is 0.99. The curves were calculated using the area coverages from Section 2.3.2.

3.4.1 Finding the best parameter values

The parameter values used by Nèmec et al. (2023) are $B_{min} = 60$ G, $B_{max} = 700$ G, and $B_{sat} = 250$ G. These values were optimized for the SFTM model with randomized spot emergence. Consequently, they may not be ideal for HMI magnetograms. When these parameters are applied to HMI magnetograms, they tend to significantly underestimate the faculae contribution to the SSI while overestimating the sunspots contribution. This discrepancy is primarily due to the relatively low B_{min} value.

To identify the best parameter values for calculating area coverage, I systematically vary B_{min}, B_{max}, and B_{sat}, and compute the SSI NV for each parameter set. These results are then compared to the variability from the SATIRE-S model for the same wavelengths. The comparison involves calculating the linear correlation coefficient and the normalized L2-distance between the computed and reference curves. The optimal parameter values are those that yield the highest correlation coefficients and the smallest L2-distances.

The L2-distance, or Euclidean distance, is a metric used to quantify the difference between two sets of data. In the context of this section, it measures the discrepancy between the SSI NV calculated from the HMI magnetograms and the variability from the SATIRE-S model. I define the normalized L2-distance between two datasets (a_i) and (b_i) as:

$$L2 = \sqrt{\frac{\sum_{i=1}^{n}[(a_i) - (b_i)]^2}{\sum_{i=1}^{n}(b_i)^2}}, \tag{3.3}$$

where n is the total number of data points – in this case, the number of days in the time series. A lower normalized L2-distance indicates that the model or method under evaluation closely matches the reference data. This suggests a higher accuracy in reproducing the variability or trend observed in the reference model. A higher normalized L2-distance signifies a greater deviation between the model's output and the reference data, indicating less accurate reproduction of the variability.

The parameter values are varied within the following ranges: $B_{min} \in [60, 710]$ G, $B_{max} \in [710, 1300]$ G, and $B_{sat} \in [250, 1200]$ G, with increments of 20 G. For each parameter set, SSI NV curves are calculated, and their correlation coefficients and L2-distances are assessed relative to the corresponding SATIRE-S curves. The parameters that produced the best results are:

- $B_{min}^{HMI} = 640$ G
- $B_{max}^{HMI} = 710$ G
- $B_{sat}^{HMI} = 310$ G

Figure 3.3 displays the SSI NV obtained using these optimal parameters. At $\lambda = 200$ nm, the method successfully reproduces the variability observed in the SATIRE-S model, achieving a correlation coefficient of 0.957 and a normalized L2-distance of 0.301. At $\lambda = 700$ nm, the correlation coefficient decreases to 0.766 and the normalized L2-distance increases to 0.654, indicating that the sunspot contribution to SSI variability is less accurately represented compared to faculae. This can be clearly noticed in the several spot transtis in the SATIRE-S model that are not captured by the method – e.g. around days 170, 240, and 300. Despite this, the results are close to the SATIRE-S variability, and the general trend is well captured, which is sufficient for the purposes of this study.

Figure 3.4 visualizes Equations 3.1 and 3.2 with the best parameter values. Each parameter plays a distinct role in calculating the area coverage of sunspots and faculae:

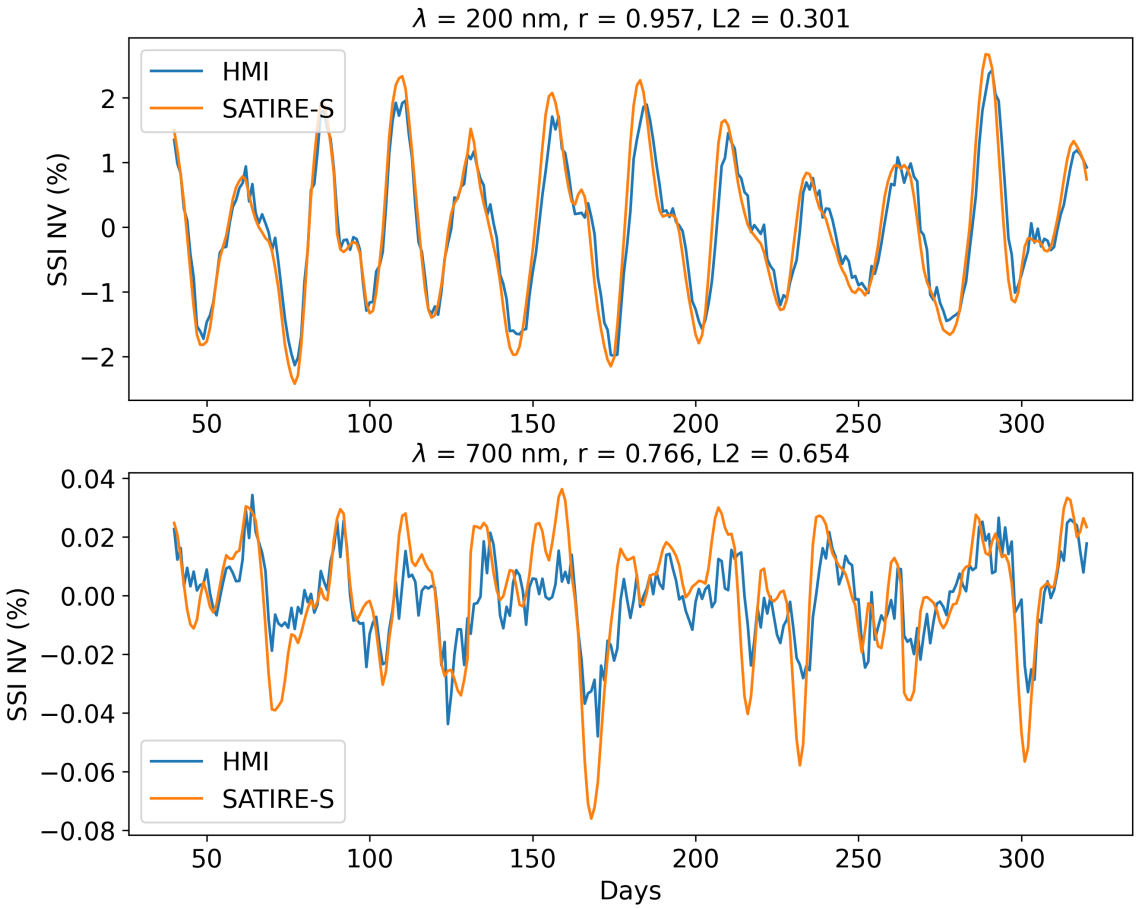

Figure 3.3: SSI normalized variability obtained from the area coverage of sunspots and faculae (labeled "HMI"), compared to the SATIRE-S normalized variability, for the optimal parameter values $B_{min}^{HMI} = 640$ G, $B_{max}^{HMI} = 710$ G, and $B_{sat}^{HMI} = 310$ G. Top: Time series at $\lambda = 200$ nm. Bottom: Time series at $\lambda = 700$ nm. The correlation coefficients (r) and the normalized L2-distances (L2) for both time series are displayed above each panel.

- $B_{min}^{HMI} = 640$ G is the magnetic field strength below which the area coverage of sunspots is zero and all magnetic field anomalies are considered faculae;
- $B_{max}^{HMI} = 710$ G is the magnetic field strength above which the area coverage of sunspots reaches one. The area coverage increases linearly with the magnetic field strength and saturates at B_{max};
- $B_{sat}^{HMI} = 310$ G is the magnetic field strength above which the area coverage of faculae reaches one. The area coverage increases linearly with the magnetic field strength and saturates at B_{sat}.

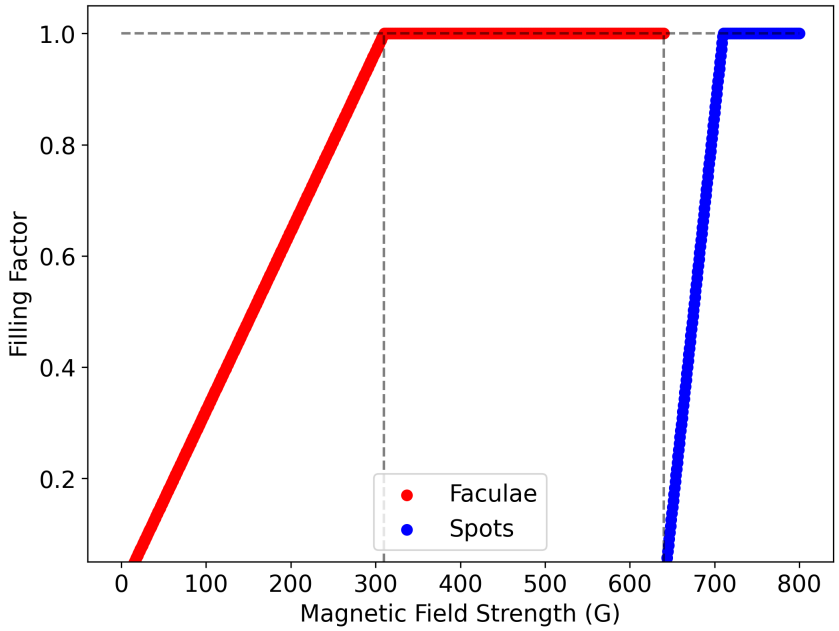

Figure 3.4: Behavior of Equations 3.1 and 3.2 for the optimal parameter values $B_{min}^{HMI} = 640$ G, $B_{max}^{HMI} = 710$ G, and $B_{sat}^{HMI} = 310$ G.

3.4.2 The role of downscaling the magnetograms

In this section, I evaluate the impact of resizing magnetograms on the estimation of the solar irradiance variability, given that FARM magnetograms do not have the high spatial resolution of HMI data. Using the optimal parameter values obtained in Section 3.4.1, I compare the SSI NV calculated from HMI magnetograms at their original resolution of 4096×4096 pixels to those obtained from magnetograms downscaled to 256×256 pixels. The comparison results are illustrated in Figure 3.5.

The analysis reveals that the SSI variability for both the original and downscaled image sizes exhibit very similar shapes and amplitudes. This consistency indicates that resizing the magnetograms does not significantly affect the estimation of solar irradiance variability. This outcome aligns with expectations, as the calculation of irradiance (described by Equations 2.2 and 2.3) is adjusted for the pixel's solid angle, thereby accommodating different image sizes.

The minimal discrepancies observed between the time series primarily occur at points of minima. These differences are minor and do not substantially impact the overall results. Consequently, downscaling the magnetograms to 256×256 pixels does not significantly affect the estimation of solar irradiance variability for the purposes of this study.

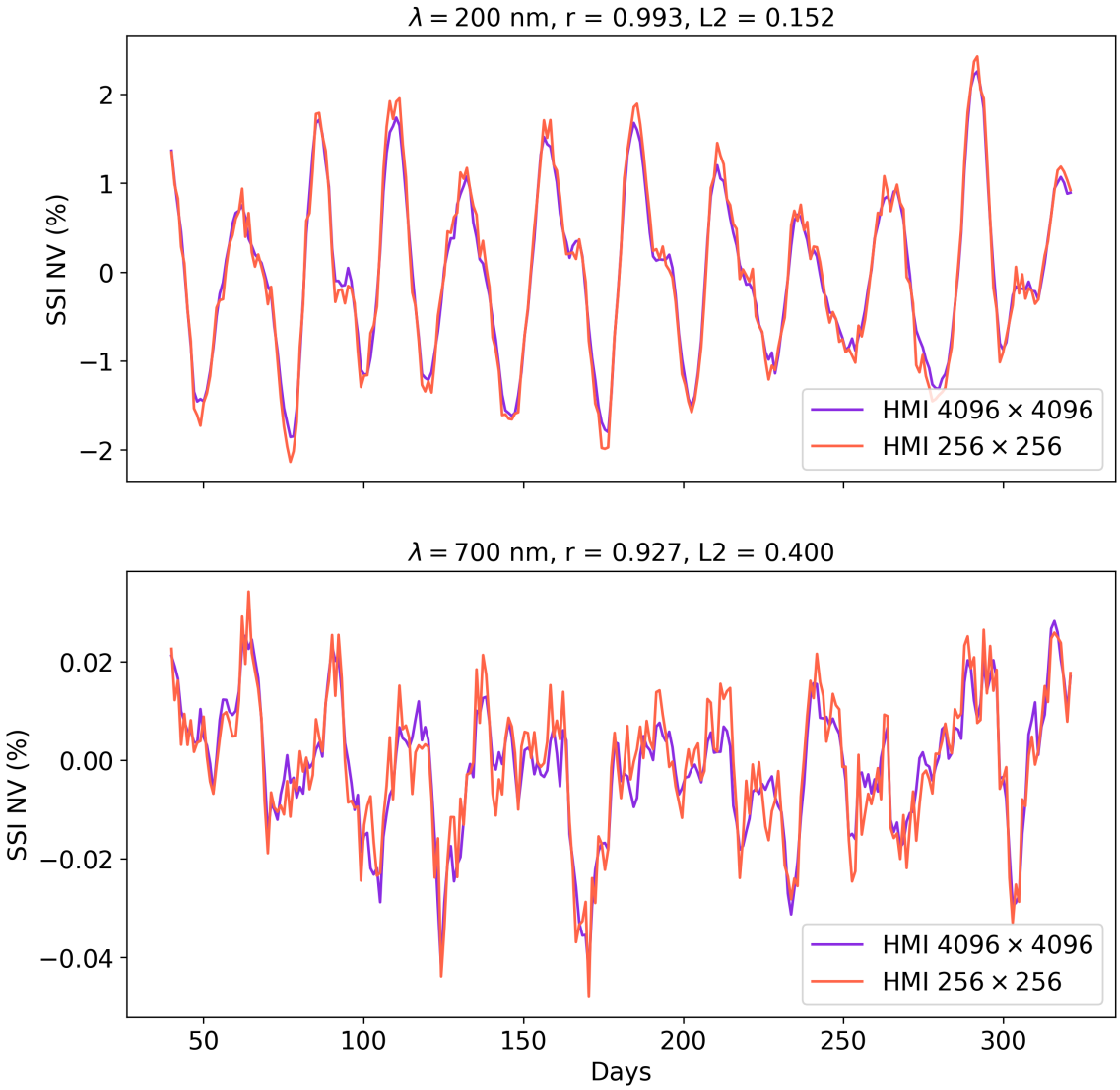

Figure 3.5: SSI normalized variability obtained from magnetograms at the original size of 4096×4096 and downscaled to 256×256. Top: Time series at $\lambda = 200\,\text{nm}$. Bottom: Time series at $\lambda = 700\,\text{nm}$. The correlation coefficients (r) and the normalized L2-distances (L2) for both time series are shown above each panel.

3.4.3 The role of Gaussian smoothing the magnetograms

In this section, I assess how Gaussian smoothing of magnetograms influences the estimation of solar irradiance variability. The resulting magnetic field maps from the SFTM model are smoothed with a Gaussian filter, because the model cannot resolve small-scale magnetic features. When a Gaussian filter is applied to an image, the values in each pixel of the image are replaced by a linear combination of its neighboring pixels. This filtering process results in the strong magnetic fields being spread out in larger areas of weaker magnetic field intensities.

Figure 3.6 provides a visual comparison between an HMI magnetogram and a Gaussian-smoothed FARM magnetogram in the Carrington coordinate frame. The HMI magnetogram, with its high spatial resolution, shows well resolved magnetic field regions, while the FARM magnetogram, after smoothing, appears blurred and less defined. The magnetic field strength in the FARM magnetogram is also notably lower, indicating that a different set of parameters is required for the area coverage calculation for FARM magnetograms.

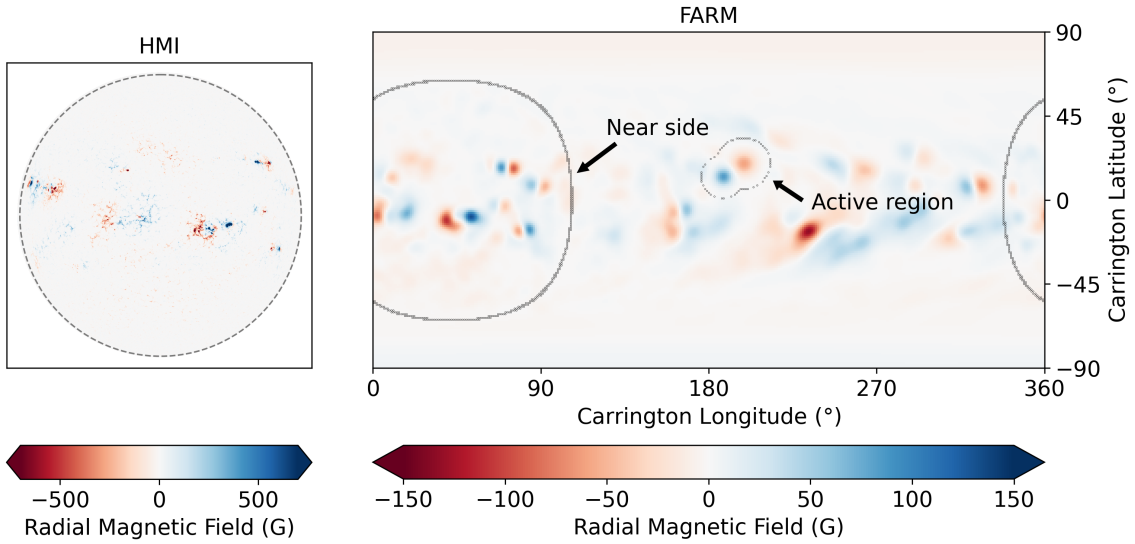

Figure 3.6: Left: HMI magnetogram at January 30th, 2015. Right: Corresponding FARM magnetogram. The near side disc and an emergent active region on the far side are approximately represented by the dashed regions. The FARM model is described by Yang et al. (2024, in preparation).

I fit the model of area coverage calculation to the FARM magnetograms by comparing the SSI NV obtained from the FARM magnetograms at the near side to the SSI NV from the SATIRE-S model, at the wavelengths of 200 nm and 700 nm. The approach is the same as in Section 3.4.1, where I vary the parameters B_{min}, B_{max}, and B_{sat}, and calculate the SSI NV, the correlation coefficient, and the normalized L2-distance for each parameter set. The optimal parameter values for the FARM magnetograms are more similar to the original values used by Nèmec et al. (2023), and are as follows:

- $B_{min}^{FARM} = 100$ G
- $B_{max}^{FARM} = 650$ G
- $B_{sat}^{FARM} = 330$ G

Figure 3.7 shows the behavior of Equations 3.1 and 3.2 using these parameters. The lower magnetic field strength values in the FARM magnetograms are reflected in the adjusted parameters B_{min} and B_{max}. The saturation value for faculae, $B_{sat}^{FARM} = 330$ G, is set higher than the minimum value $B_{min}^{FARM} = 100$ G, indicating that a pixel cannot be completely occupied by a facula, which contrasts with the situation in HMI magnetograms. This is consistent with the effect of Gaussian smoothing, which spreads the magnetic field over a larger area. Following the same principle, a pixel rarely contains only a sunspot, given that $B_{max}^{FARM} = 650$ G is a relatively large value for the FARM magnetograms.

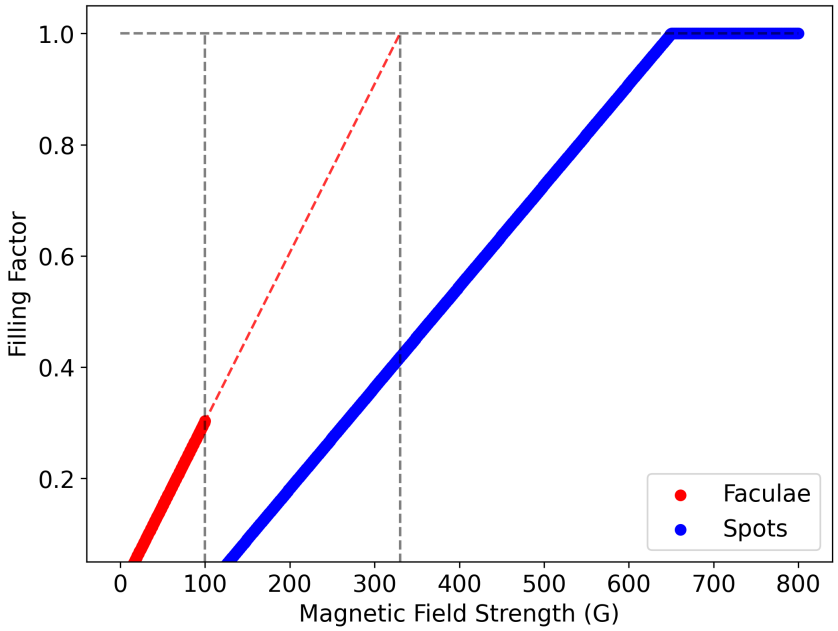

Figure 3.7: Behavior of Equations 3.1 and 3.2 for the FARM magnetograms using the optimal parameter values $B_{min}^{FARM} = 100$ G, $B_{max}^{FARM} = 650$ G, and $B_{sat}^{FARM} = 330$ G. The red dashed line shows the extrapolation of the faculae filling factor until it reaches B_{sat}^{FARM}.

The SSI NV obtained from the FARM magnetograms at the near side of the Sun, using the optimal parameters, is compared to the SSI NV from the SATIRE-S model in Figure 3.8. The correlation coefficients and the L2-distances are similar to those for the HMI magnetograms, with an improvement in the results at $\lambda = 700$ nm. This indicates that it is feasible to estimate solar irradiance variability using Gaussian-smoothed magnetograms, as the general trends are accurately reproduced.

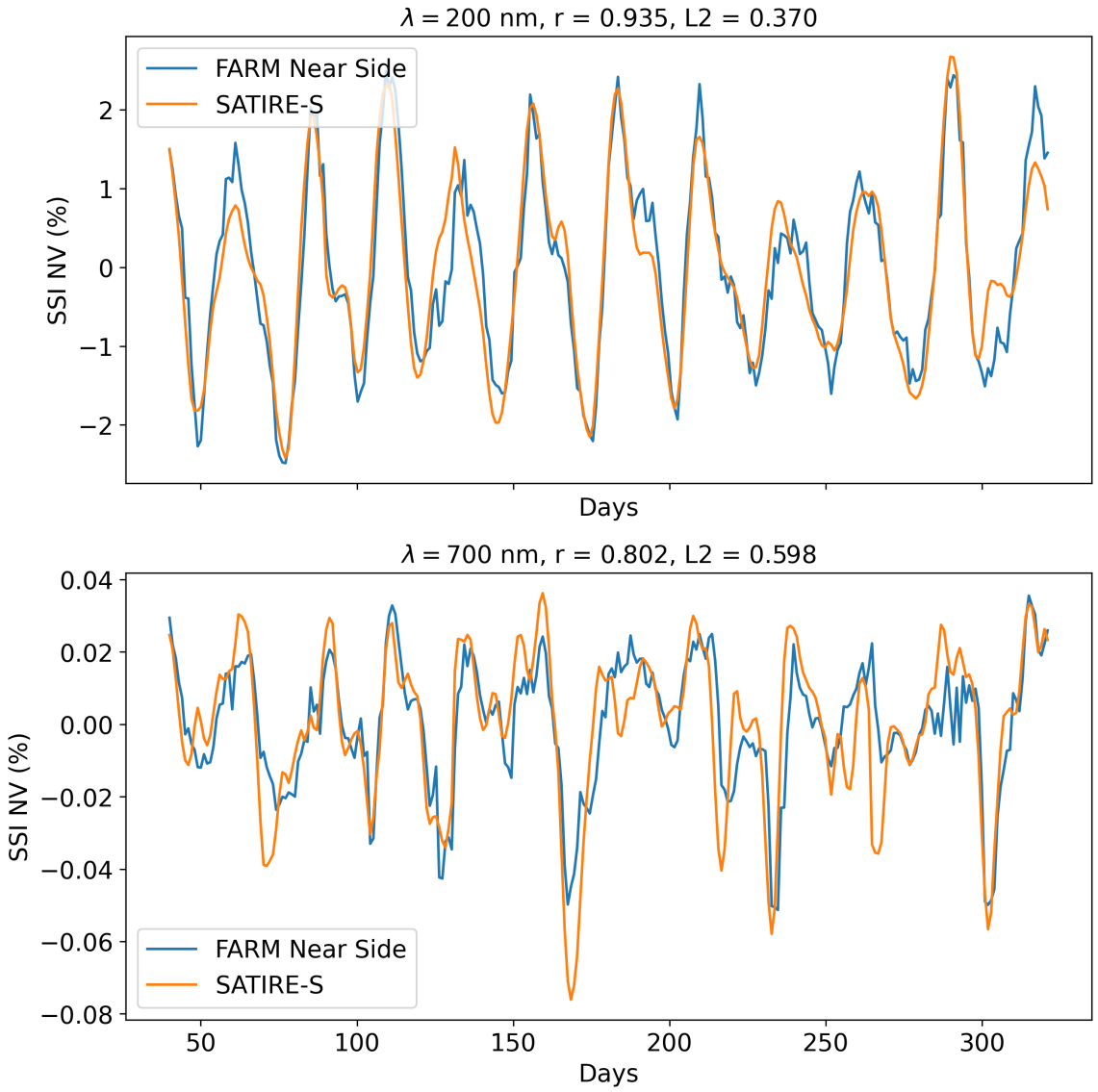

Figure 3.8: SSI normalized variability for the FARM magnetograms at the near side using $B_{min}^{FARM} = 100$ G, $B_{max}^{FARM} = 650$ G, and $B_{sat}^{FARM} = 330$ G, compared to the SSI normalized variability from the SATIRE-S model. Top: Time series at $\lambda = 200$ nm. Bottom: Time series at $\lambda = 700$ nm. The correlation coefficients (r) and the normalized L2-distances (L2) for both time series are shown above each panel.

3.5 Estimating SSI variability at Mars using FARM magnetograms

The final goal of this work is to estimate the SSI variability from different planetary vantage points, using FARM magnetograms. Mars is selected for this case study, as it is the only planet with SSI data available for comparison. By using the positional parameters of Mars – i.e., the Earth-Sun-Mars angle (ϕ_M), the orbital inclination of Mars (θ_M), and the distance from Mars to the Sun (r_M) –, it is possible to calculate the visible solar disc at Mars for each day in 2015.

Figure 3.9 presents the positional parameters for Mars throughout 2015. Notice that ϕ_M varies between approximately 75° and 250°, which means that an observer at Mars is always looking at a very different solar disc than an observer at Earth, i.e., located at $\phi = 0°$.

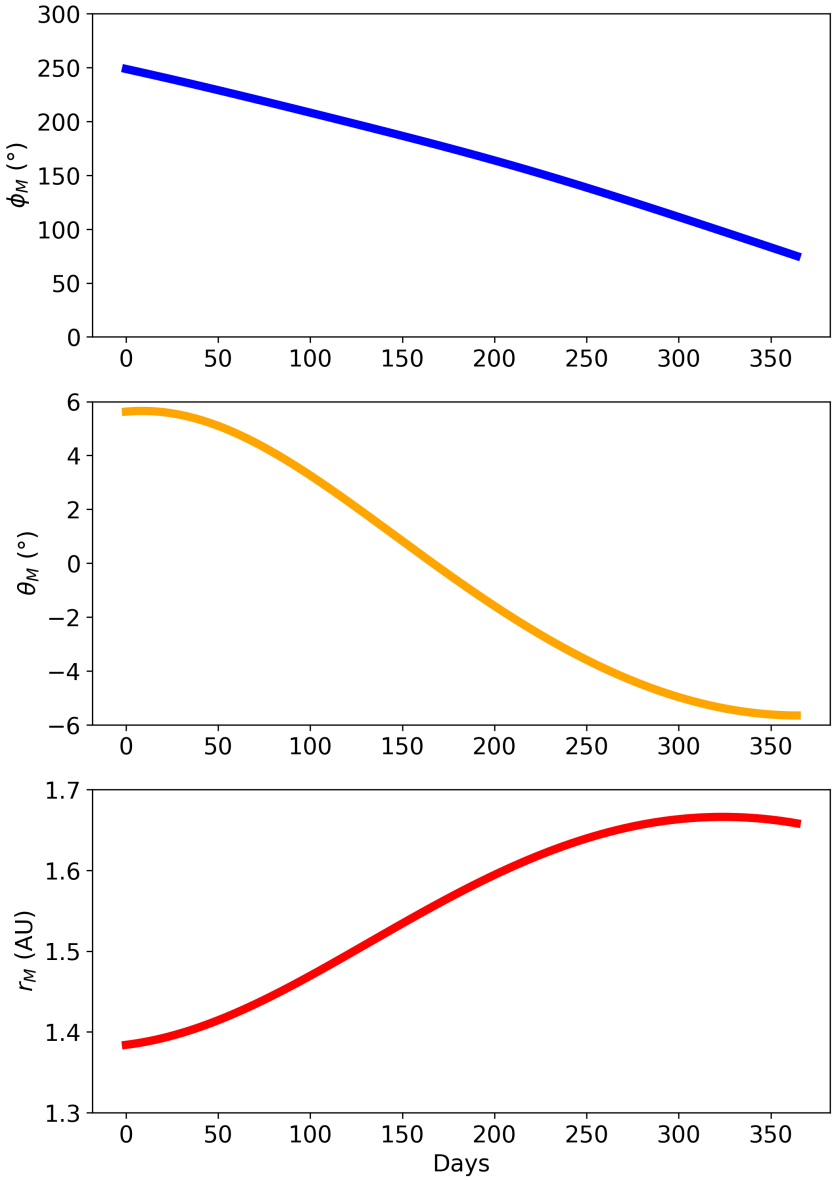

Figure 3.9: Positional parameters for Mars in 2015: Earth-Sun-Mars angle (ϕ_M), orbital inclination of Mars (θ_M), and distance from Mars to the Sun (r_M).

3.5.1 Comparison to EUVM data

In this section, I compare the SSI NV obtained from the FARM magnetograms for an observer at Mars with the SSI NV from the EUVM data at Mars. The area coverages of sunspots and faculae are calculated for an observer at Mars using the best parameter values derived for the FARM magnetograms. This comparison serves to validate our estimation method and assess the feasibility of using FARM magnetograms to estimate SSI variability at Mars.

The EUVM dataset, which is composed of solar irradiance at Mars across the wavelength range of 0.1 to 190 nm, is particularly relevant for understanding Mars's upper atmospheric processes. For this analysis, I focus on wavelengths 180 nm and 190 nm, as they are close to the 200 nm wavelength used in previous sections.

Figure 3.10 illustrates the comparison between SSI NV derived from FARM magnetograms and the SSI NV from EUVM data at Mars. The correlation coefficients and L2-distances between the time series are provided above each panel.

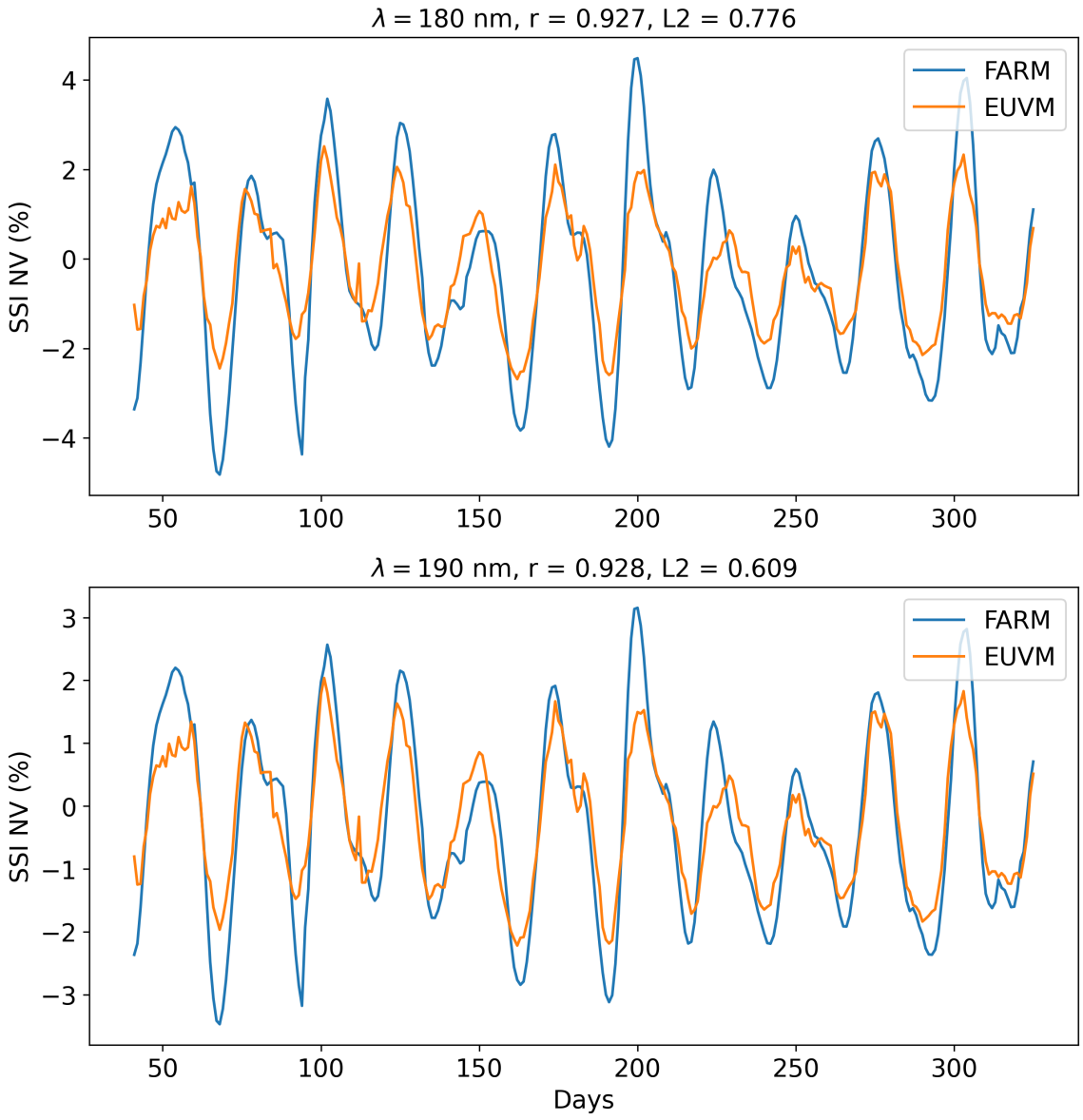

Figure 3.10: Comparison of the SSI normalized variability from FARM magnetograms and EUVM data at Mars.

Figure 3.10 demonstrates that the SSI NV obtained from FARM magnetograms for Mars aligns well with the EUVM data in terms of overall variability trends, as indicated by the high correlation coefficients. However, discrepancies are evident in the amplitude of variability, with higher normalized L2-distances compared to results obtained for the near side of the Sun.

For shorter wavelengths not covered in this study, the L2-distances are even larger. These discrepancies are anticipated due to the limitations of the intensity models used in this work (Unruh, Solanki, and Fligge 1999), which rely on the ATLAS9 radiative transfer code (Kurucz 1992) under the assumption of LTE. Tagirov et al. (2019) showed that chromospheric layers need to be included for accurate modeling of the solar spectrum below 200 nm, as photons originating in these layers significantly affect the solar irradiance in this wavelength range. Modeling these layers accurately requires a non-LTE approach, making the current LTE-based model less reliable for wavelengths shorter than 200 nm.

3.5.2 Interpolating FARM magnetograms to Mars

In this section, I compare two methods of estimating SSI NV at Mars: one using FARM magnetograms observed directly from Mars, and the other using FARM magnetograms observed from Earth and interpolated to Mars following the "lighthouse" model. This comparison pinpoints the issues associated with the interpolation method for estimating SSI variability at different planetary vantage points and complements the findings discussed in Chapter 2.

The interpolation method described in Section 2.4.2 is employed to estimate the variability of the TSI and the S-index at Mars based on data from FARM magnetograms observed at Earth. The results are compared to the variability derived directly from FARM magnetograms observed from Mars. These comparisons are illustrated in Figure 3.11, with correlation coefficients and L2-distances provided at above each panel.

The S-index variability obtained for Mars from the FARM magnetograms closely matches the variability calculated by interpolating FARM magnetograms from Earth to Mars. The high correlation coefficient and low L2-distance indicate that the interpolation method effectively captures the variability predominantly influenced by faculae. This result supports the utility of interpolation for estimating faculae-driven variability.

The results for TSI NV show a different outcome. The low correlation coefficient of 0.489 and the high L2-distance of 0.903 suggest that the interpolation method performs less well in estimating TSI variability, which is primarily driven by sunspot activity. This discrepancy is expected and aligns with the problems discussed in Section 2.4.2. The interpolation method does not account for the emergence and evolution of active regions on the far side of the Sun. In contrast, the FARM magnetograms incorporate this information, providing a more accurate representation of TSI variability that includes the contribution of far side active regions.

The findings emphasizes the limitations of the interpolation method in capturing sunspot-related variability due to its exclusion of far side active regions. However, for faculae-dominated variability, the interpolation method proves to be quite effective. The FARM magnetograms for Mars provide a more realistic representation of the visible solar disc by incorporating data from the far side of the Sun. This perspective helps provide more accurate estimates of solar irradiance variability from Mars, as demonstrated by the results obtained Figure 3.11, affirming the importance of utilizing such detailed and far-side-inclusive data for reliable assessments.

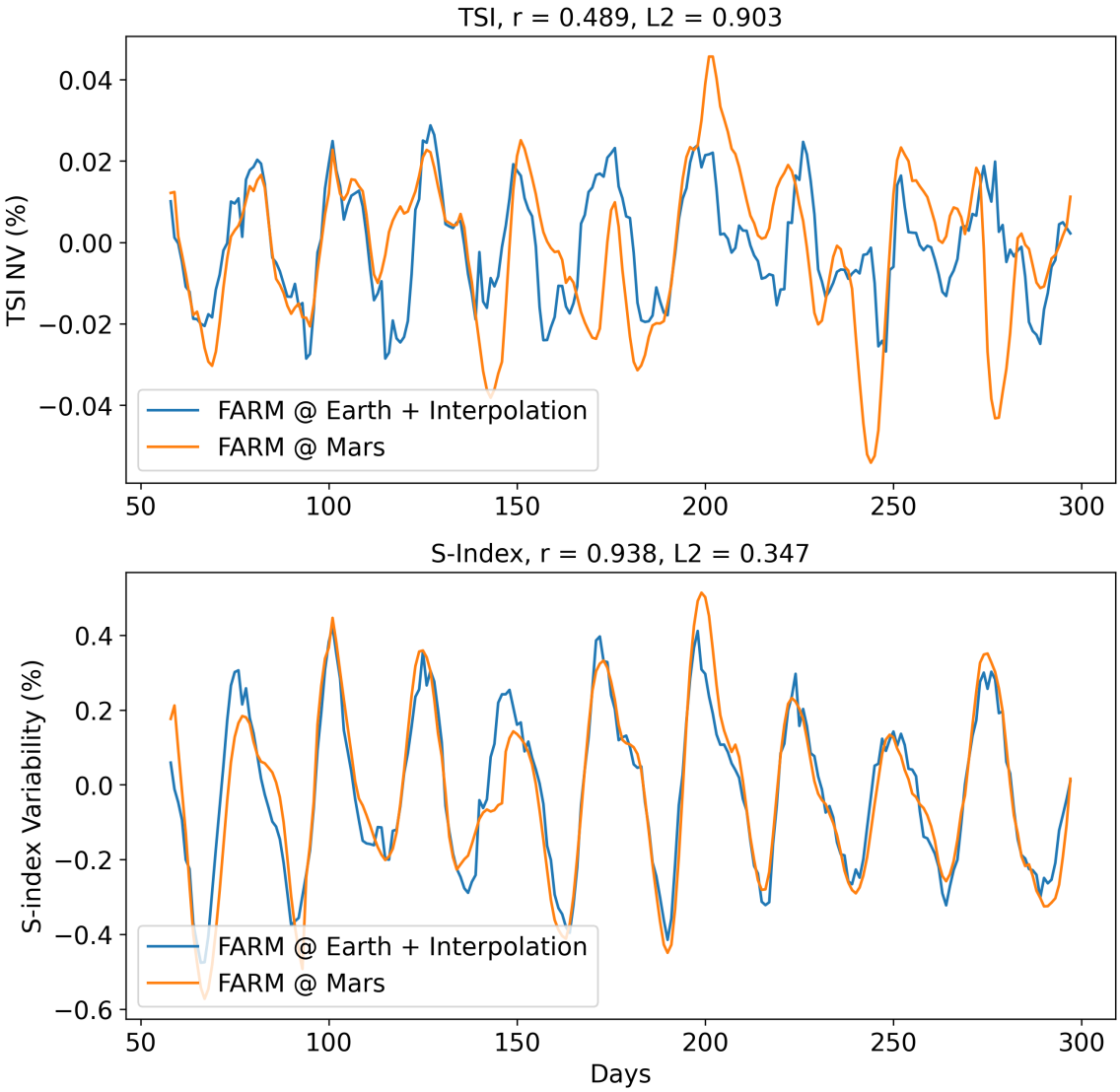

Figure 3.11: Comparison of SSI normalized variability between FARM magnetograms for an observer at Mars and FARM magnetograms for an observer at Earth, interpolated to Mars.

3.6 Summary and Conclusions

In this chapter, I have demonstrated that it is feasible to estimate solar irradiance variability from other vantage points in the Solar System using only magnetic field data, without relying on additional observational sources such as intensity continuum maps. This finding shows that magnetic field information alone can provide sufficiently accurate estimates of solar irradiance variability in contexts where comprehensive datasets like those used in the SATIRE-S model are unavailable.

Firstly, I estimated the area coverage of sunspots and faculae from near side HMI magnetograms using linear relationships between magnetic field strength and area coverage, following the method outlined by Nèmec et al. (2023). By comparing these estimates to those obtained from the SATIRE-S model, I confirmed that magnetic field data alone can reproduce solar irradiance variability across different wavelengths in a sufficiently accurate manner for the purposes of this study. The optimal parameter values for calculating area coverage were determined to be $B_{min}^{HMI} = 640$ G, $B_{max}^{HMI} = 710$ G, and $B_{sat}^{HMI} = 310$ G.

Secondly, I investigated the effect of downscaling HMI magnetograms to a resolution comparable to that of FARM magnetograms on the estimation of SSI variability. The downscaling was performed to ensure consistency in resolution between datasets. My analysis demonstrated that this process does not significantly impact the accuracy of SSI variability estimates in the rotational timescale. This result allows for meaningful comparisons between the different datasets, ensuring that the variability estimates derived from FARM magnetograms and HMI magnetograms remain reliable and comparable.

Thirdly, I explored the use of Gaussian-smoothed FARM magnetograms for estimating SSI variability. The FARM model, which includes information on large-scale solar surface flows and far side active regions, provided accurate estimates of sunspot and faculae coverage even from smoothed data. This demonstrates the robustness of using smoothed FARM magnetograms for variability estimation.

Fourthly, I examined the potential of estimating SSI variability at Mars using FARM magnetograms. Given that Mars is the only planet with available SSI data for comparison, this study offers valuable insights into solar irradiance variability beyond Earth. While there were some discrepancies in the amplitude of variability, especially at wavelengths below 200 nm, the general trends were accurately captured. These discrepancies are expected due to non-LTE effects and limitations of the intensity models used.

Finally, I compared the SSI variability estimated directly from FARM magnetograms at Mars with that obtained by interpolating FARM magnetograms from Earth to Mars, utilizing the "lighthouse" model. This comparison highlighted the effectiveness of interpolation for estimating faculae-driven variability, as evidenced by good agreement with the S-index results. However, the interpolation method showed limitations for sunspot-driven TSI variability, pinpointing the value of including far side data for more accurate estimations.

Overall, while the methodology employed in this study is not intended to surpass the accuracy of the SATIRE-S model, it provides sufficiently good estimates of solar irradiance variability for the purpose of studying the far side of the Sun. This approach proves effective in scenarios where comprehensive datasets are not available, offering valuable insights into solar activity and variability across different planetary vantage points.

Chapter 4

Conclusions and Outlook

Here, I summarize the key findings from Chapters 2 and 3, discuss the implications of these results, and outline potential directions for future research. The objective is to assess what has been achieved, to identify promising avenues for further study, and to address current limitations.

Summary of findings

Chapter 2 introduces a SATIRE-inspired method for estimating spectral (SSI) and total solar irradiance (TSI) variability at various vantage points in the Solar System. This method utilizes the area coverage of sunspots and faculae derived from synthetic solar surface magnetograms to account for the emergence and evolution of magnetic features on the solar surface. By evaluating the TSI and the S-index (a proxy for UV variability) at four Earth-Sun-planet angles ($\phi = 0°, 90°, 180°$, and $270°$) during periods of high and low solar activity, the study reveals that a simple phase shift of the data is insufficient for accurate solar irradiance estimation.

The SATIRE-inspired approach is also compared with the traditional interpolation method – or "lighthouse" method –, which assumes that irradiance variability is solely due to solar rotation (Thiemann et al. 2017). The results indicate a strong correlation between the SATIRE-inspired approach and the interpolation method for the S-index. However, this correlation does not extend to the TSI. This discrepancy is due to the short-lived nature of sunspots, which evolve on a timescale of days and, therefore, are not properly captured by the interpolation method. The results indicate that the SATIRE-inspired approach is more accurate than the interpolation method for estimating solar irradiance variability at different planetary vantage points.

Chapter 3 extends this work by exploring the viability of using low spatial resolution magnetograms to estimate the area coverages of sunspots and faculae. This investigation serves as a proof-of-concept for reconstructing solar irradiance variability using FARM magnetograms, which incorporate information on far side active regions based on helioseismic maps (Yang et al. 2024, in preparation). The study follows several steps to identify potential information loss when transitioning from high-resolution magnetograms to FARM magnetograms. Initially, the SATIRE-S approach is applied to HMI magnetograms without noise correction, intensity continuum images, or further refinements which are used in SATIRE-S. Next, the transition is made from high resolution HMI magnetograms to low resolution HMI magnetograms. Finally, the impact of Gaussian smoothing on the magnetograms is assessed.

The study then compares the SSI variability obtained from FARM magnetograms for Mars with SSI variability from EUVM data, finding good agreement. I also compare the SSI variability estimated directly from FARM magnetograms at Mars with that obtained by interpolating FARM magnetograms from Earth to Mars. The results show that the interpolation method is effective for estimating faculae-driven variability but less accurate for sunspot-driven variability due to the lack of far side active regions. These findings underscore the importance of using comprehensive, far side-inclusive data for accurate solar irradiance variability assessments from different planetary vantage points.

Significance of this work

This work provides a foundation for predicting solar irradiance values at other planets in the Solar System, which has significant implications for atmospheric studies, planetary climate modeling, and space weather. Accurate estimations of solar irradiance variability can improve our understanding of the effects of solar activity on planetary atmospheres. This work also highlights the importance of using detailed, far side-inclusive data for reliable assessments of solar irradiance variability at different planetary vantage points.

Future directions

Validation of FARM model

The FARM model has shown significant promise in estimating the emergence of active regions on the far side of the Sun. However, further validation is necessary to confirm its accuracy and reliability. This validation is crucial for assessing the effectiveness of the FARM model in estimating solar irradiance and its variability. A straightforward approach, as proposed by Yang et al. (2023), involves comparing the FARM model results with observational data from the following sources:

(1) The Polarimetric and Helioseismic Imager (PHI, Solanki et al. 2020) onboard the Solar Orbiter spacecraft (Müller et al. 2020): PHI offers high-resolution magnetograms and intensity continuum images, which are invaluable for validating the FARM model. However, due to the complex orbit of the Solar Orbiter mission, these observations are not available on a regular basis.

(2) The Photospheric Magnetic field Imager onboard the Vigil spacecraft (https://www.mps.mpg.de/pmi): Scheduled for launch in 2031, the Vigil mission will provide continuous vector magnetogram observations of the Sun from the L5 Lagrange point. This unique vantage point offers a view of the Sun that enables the observation of solar regions before they rotate to face Earth (Vourlidas 2015).

Another method for validating the FARM model involves using it to predict photospheric magnetic fields or solar spectral irradiance over short timescales – i.e., a few days – at Earth. These predictions can then be compared to observations from the HMI instrument or SSI observations. Given the extensive dataset available from HMI magnetograms, this comparison can be conducted over a large number of days, providing a robust validation framework for the FARM model.

Limitations of the interpolation method

While the current interpolation method is effective for estimating UV/EUV variability at other planets, it is less reliable for TSI or wavelengths in the VIS and IR ranges. These ranges are relevant for planetary studies as they affect temperatures and chemical processes in the planets of the Solar System – see, e.g., absorption of broad-spectrum solar radiation by CO_2 ice on Mars (Chinnery et al. 2020) and absorption of solar IR radiation by atmospheric CO_2 on Venus (Crisp 1986). More accurate methods for these ranges could improve our understanding of planetary systems and their responses to solar variability.

Improvements in area coverage estimation

The linear relationship between magnetic field strength and area coverage of sunspots and faculae is a simplification of the complex physical processes on the Sun. Future research could develop more sophisticated and accurate models for estimating solar irradiance from FARM magnetograms. Preliminary results suggest that neural network models may offer promising improvements in predicting sunspot area coverage from magnetograms, though these models require further refinement before they can be used reliably for solar irradiance variability estimation (see Appendix 4).

Addressing LTE assumptions

A major limitation of this work is the assumption of local thermodynamic equilibrium (LTE) in intensity models. This assumption is not valid for wavelengths below 200 nm, where non-LTE effects become significant, particularly for photons originating in chromospheric layers. To improve accuracy for these wavelengths, future work should explore models that account for non-LTE effects, such as those proposed by Tagirov et al. (2019), to provide more reliable estimates of solar irradiance variability.

In summary, while this work has provided valuable insights and methodologies for estimating solar irradiance variability, addressing its limitations and exploring new methods will be important for advancing our understanding of solar activity and its impact on planetary atmospheres. By refining existing models, incorporating new data sources, and exploring novel approaches, future research can enhance our knowledge of solar variability and its effects on the Solar System.

Improving Mars atmospheric modeling through accurate estimates of solar irradiance

Key tools used to study Martian atmospheric dynamics are General Circulation Models (GCM, e.g., Hartogh et al. 2005), which are sophisticated computer models that simulate the circulation of the planet's atmosphere based on physical principles. These models require accurate input parameters, including spectral solar irradiance, to produce reliable predictions. With precise solar irradiance data, GCMs can more accurately simulate seasonal and diurnal temperature variations, atmospheric circulation patterns, and the distribution of dust and aerosols in the Martian atmosphere. This, in turn, helps improve our knowledge on weather patterns, surface-atmosphere interactions, and the potential habitability of Mars. Improved GCM simulations also aid in the interpretation of data from current and future Mars missions, providing a more comprehensive picture of the planet's atmospheric behavior and evolution.

Combining solar irradiance models at Mars with data from the HOPE mission

The HOPE mission (Amiri et al. 2022), designed to study the Martian atmosphere and climate (Almatroushi et al. 2021), utilizes a combination of remote sensing and in-situ measurements. This mission provides invaluable data on the composition, structure, and dynamics of the Martian atmosphere, including insights into dust storms, water vapor distribution, and other atmospheric constituents. By integrating data from the HOPE mission with accurate estimates of solar irradiance variability at Mars, we can achieve a more comprehensive understanding of the effects of solar forcing on the Martian atmosphere. Potential works include:

- Linking Solar Irradiance to Global Temperatures: Utilizing data from the Emirates Mars Infrared Spectrometer (Edwards et al. 2021), we can correlate solar irradiance at Mars with observed global temperature variations, enhancing our understanding of how solar energy influences Martian climate patterns.
- Investigating Solar Variability's Impact on Atmospheric Phenomena: Using data from the Emirates Exploration Imager (Jones et al. 2021), we can investigate how variability in solar irradiance affect the occurrence and intensity of dust storms and the behavior of water vapor in the Martian atmosphere, providing insights into weather and climate changes.
- Studying Atmospheric Escape Rates: With data from the Emirates Mars Ultraviolet Spectrometer (Holsclaw et al. 2021), we can examine how variability in solar irradiance influences the escape rates of atmospheric components, improving the knowledge on the long-term atmospheric evolution of the Martian atmosphere.

Bibliography

Almatroushi, Hessa et al. (2021). "Emirates Mars Mission Characterization of Mars Atmosphere Dynamics and Processes". In: *Space Science Reviews* 217.8, 89, p. 89. DOI: 10.1007/s11214-021-00851-6.

Amiri, H. E. S. et al. (2022). "The Emirates Mars Mission". In: *Space Science Reviews* 218.1, 4, p. 4. DOI: 10.1007/s11214-021-00868-x.

Baumann, Ingo Jens (2005). "Magnetic flux transport on the Sun". PhD thesis. Georg August University of Gottingen, Germany.

Buehler, Stefan A. et al. (2018). "ARTS, the Atmospheric Radiative Transfer Simulator - version 2.2, the planetary toolbox edition". In: *Geoscientific Model Development* 11.4, pp. 1537–1556. DOI: 10.5194/gmd-11-1537-2018.

Cameron, R. H. et al. (2010). "Surface Flux Transport Modeling for Solar Cycles 15-21: Effects of Cycle-Dependent Tilt Angles of Sunspot Groups". In: *The Astrophysical Journal* 719.1, pp. 264–270. DOI: 10.1088/0004-637X/719/1/264. arXiv: 1006.3061 [astro-ph.SR].

Castelli, F. and R. L. Kurucz (1994). "Model atmospheres for Vega." In: *Astronomy & Astrophysics* 281, pp. 817–832.

Catling, D.C. (2015). "10.13 - Planetary Atmospheres". In: *Treatise on Geophysics (Second Edition)*. Ed. by Gerald Schubert. Second Edition. Oxford: Elsevier, pp. 429–472. ISBN: 978-0-444-53803-1. DOI: https://doi.org/10.1016/B978-0-444-53802-4.00185-8. URL: https://www.sciencedirect.com/science/article/pii/B9780444538024001858.

Chinnery, H. E. et al. (2020). "The Penetration of Solar Radiation Into Granular Carbon Dioxide and Water Ices of Varying Grain Sizes on Mars". In: *Journal of Geophysical Research: Planets* 125.4, e06097, e06097. DOI: 10.1029/2019JE006097.

Clancy, R. T. et al. (2000). "An intercomparison of ground-based millimeter, MGS TES, and Viking atmospheric temperature measurements: Seasonal and interannual variability of temperatures and dust loading in the global Mars atmosphere". In: *Journal of Geophysical Research* 105.E4, pp. 9553–9572. DOI: 10.1029/1999JE001089.

Crisp, D. (1986). "Radiative forcing of the Venus mesosphere I. Solar fluxes and heating rates". In: *Icarus* 67.3, pp. 484–514. DOI: 10.1016/0019-1035(86)90126-0.

De Oliveira, Isabela (2024). *Data from: Estimation of solar irradiance in the ecliptic plane using synthetic solar surface magnetograms*. DOI: 10.5281/zenodo.10630214. URL: https://doi.org/10.5281/zenodo.10630214.

DeLand, Matthew and Sergey Marchenko (2013). "The solar chromospheric Ca and Mg indices from Aura OMI". In: *Journal of Geophysical Research (Atmospheres)* 118.8, pp. 3415–3423. DOI: 10.1002/jgrd.50310.

Edwards, Christopher S. et al. (2021). "The Emirates Mars Mission (EMM) Emirates Mars InfraRed Spectrometer (EMIRS) Instrument". In: *Space Science Reviews* 217.7, 77, p. 77. DOI: 10.1007/s11214-021-00848-1.

Eparvier, F. G. et al. (2015). "The Solar Extreme Ultraviolet Monitor for MAVEN". In: *Space Science Reviews* 195.1-4, pp. 293–301. DOI: 10.1007/s11214-015-0195-2.

Ermolli, I. et al. (2013). "Recent variability of the solar spectral irradiance and its impact on climate modelling". In: *Atmospheric Chemistry & Physics* 13.8, pp. 3945–3977. DOI: 10.5194/acp-13-3945-201310.5194/acpd-12-24557-2012. arXiv: 1303.5577 [astro-ph.SR].

Fligge, M., S. K. Solanki, and Y. C. Unruh (2000). "Modelling irradiance variations from the surface distribution of the solar magnetic field". In: *Astronomy & Astrophysics* 353, pp. 380–388.

Floyd, Linton et al. (2003). "11 years of solar UV irradiance measurements from UARS". In: *Solar Variability as an Input to the Earth's Environment*. Ed. by Andrew Wilson. Vol. 535. ESA Special Publication, pp. 195–203.

Foukal, P. and J. Lean (1988). "Magnetic Modulation of Solar Luminosity by Photospheric Activity". In: *Astrophysical Journal* 328, p. 347. DOI: 10.1086/166297.

Fox, Jane L., Marina I. Galand, and Robert E. Johnson (2008). "Energy Deposition in Planetary Atmospheres by Charged Particles and Solar Photons". In: *Space Science Reviews* 139.1-4, pp. 3–62. DOI: 10.1007/s11214-008-9403-7.

Fröhlich, Claus and Judith Lean (1998). "The Sun's total irradiance: Cycles, trends and related climate change uncertainties since 1976". In: *Geophysical Research Letters* 25.23, pp. 4377–4380. DOI: 10.1029/1998GL900157.

Fröhlich, Claus et al. (1997). "First Results from VIRGO, the Experiment for Helioseismology and Solar Irradiance Monitoring on SOHO". In: *Solar Physics* 170.1, pp. 1–25. DOI: 10.1023/A:1004969622753.

Gray, L. J. et al. (2010). "Solar Influences on Climate". In: *Reviews of Geophysics* 48.4, RG4001, RG4001. DOI: 10.1029/2009RG000282.

Haberle, Robert M. et al. (2019). "Documentation of the NASA/Ames Legacy Mars Global Climate Model: Simulations of the present seasonal water cycle". In: *Icarus* 333, pp. 130–164. DOI: 10.1016/j.icarus.2019.03.026.

Hale, George E. et al. (1919). "The Magnetic Polarity of Sun-Spots". In: *Astrophysical Journal* 49, p. 153. DOI: 10.1086/142452.

Harder, Jerald et al. (2005). "The Spectral Irradiance Monitor: Scientific Requirements, Instrument Design, and Operation Modes". In: *Solar Physics* 230.1-2, pp. 141–167. DOI: 10.1007/s11207-005-5007-5.

Hartogh, Paul et al. (2005). "Description and climatology of a new general circulation model of the Martian atmosphere". In: *Journal of Geophysical Research: Planets* 110.E11. DOI: https://doi.org/10.1029/2005JE002498. eprint: https://agupubs.onlinelibrary.wiley.com/doi/pdf/10.1029/2005JE002498. URL: https://agupubs.onlinelibrary.wiley.com/doi/abs/10.1029/2005JE002498.

Hohenegger, Cathy et al. (Jan. 2023). "ICON-Sapphire: simulating the components of the Earth system and their interactions at kilometer and subkilometer scales". In: *Geoscientific Model Development* 16.2, pp. 779–811. DOI: 10.5194/gmd-16-779-2023.

Holsclaw, Gregory M. et al. (2021). "The Emirates Mars Ultraviolet Spectrometer (EMUS) for the EMM Mission". In: *Space Science Reviews* 217.8, 79, p. 79. DOI: 10.1007/s11214-021-00854-3.

Jakosky, B. M. et al. (2015). "The Mars Atmosphere and Volatile Evolution (MAVEN) Mission". In: *Space Science Reviews* 195.1-4, pp. 3–48. DOI: 10.1007/s11214-015-0139-x.

Jiang, J. et al. (2011). "The solar magnetic field since 1700. II. Physical reconstruction of total, polar and open flux". In: *Astronomy & Astrophysics* 528, A83, A83. DOI: 10.1051/0004-6361/201016168. arXiv: 1102.1270 [astro-ph.SR].

Jones, A. R. et al. (2021). "The Emirates Exploration Imager (EXI) Instrument on the Emirates Mars Mission (EMM) Hope Mission". In: *Space Science Reviews* 217.8, 81, p. 81. DOI: 10.1007/s11214-021-00852-5.

Keller, C. U. et al. (2004). "On the Origin of Solar Faculae". In: *The Astrophysical Journal* 607.1, pp. L59–L62. DOI: 10.1086/421553.

Kopp, Greg and Judith L. Lean (2011). "A new, lower value of total solar irradiance: Evidence and climate significance". In: *Geophysical Research Letters* 38.1, L01706, p. L01706. DOI: 10.1029/2010GL045777.

Krivova, N. A., S. K. Solanki, and Y. C. Unruh (2011). "Towards a long-term record of solar total and spectral irradiance". In: *Journal of Atmospheric and Solar-Terrestrial Physics* 73.2-3, pp. 223–234. DOI: 10.1016/j.jastp.2009.11.013. arXiv: 0911.4002 [astro-ph.SR].

Krivova, N. A. et al. (2003). "Reconstruction of solar irradiance variations in cycle 23: Is solar surface magnetism the cause?" In: *Astronomy & Astrophysics* 399, pp. L1–L4. DOI: 10.1051/0004-6361:20030029.

Kurucz, R. L. (1992). "Remaining Line Opacity Problems for the Solar Spectrum". In: *Revista Mexicana de Astronomia y Astrofisica* 23, p. 187.

Lean, Judith (1997). "The Sun's Variable Radiation and Its Relevance For Earth". In: *Annual Review of Astronomy and Astrophysics* 35, pp. 33–67. DOI: 10.1146/annurev.astro.35.1.33.

Leka, K. D., G. Barnes, and E. L. Wagner (2017). "Evaluating (and Improving) Estimates of the Solar Radial Magnetic Field Component from Line-of-Sight Magnetograms". In: *Solar Physics* 292.2, 36, p. 36. DOI: 10.1007/s11207-017-1057-8. arXiv: 1701.04836 [astro-ph.SR].

Lemen, James R. et al. (2012). "The Atmospheric Imaging Assembly (AIA) on the Solar Dynamics Observatory (SDO)". In: *Solar Physics* 275.1-2, pp. 17–40. DOI: 10.1007/s11207-011-9776-8.

Lindsey, C. and D. C. Braun (2000). "Seismic Images of the Far Side of the Sun". In: *Science* 287.5459, pp. 1799–1801. DOI: 10.1126/science.287.5459.1799.

"Chapter 2 - Solar Radiation at the Top of the Atmosphere" (2002). In: *An Introduction to Atmospheric Radiation*. Ed. by K.N. Liou. Vol. 84. International Geophysics. Academic Press, pp. 37–64. DOI: https://doi.org/10.1016/S0074-6142(02)80017-1. URL: https://www.sciencedirect.com/science/article/pii/S0074614202800171.

Müller, D. et al. (2017). "JHelioviewer - Time-dependent 3D visualisation of solar and heliospheric data". In: *Astronomy & Astrophysics* 606, A10. DOI: 10.1051/0004-6361/201730893. URL: https://doi.org/10.1051/0004-6361/201730893.

Müller, D. et al. (2020). "The Solar Orbiter mission. Science overview". In: *Astronomy & Astrophysics* 642, A1, A1. DOI: 10.1051/0004-6361/202038467. arXiv: 2009.00861 [astro-ph.SR].

Nèmec, N. E. et al. (2020). "Power spectra of solar brightness variations at various inclinations". In: *Astronomy & Astrophysics* 636, A43, A43. DOI: 10.1051/0004-6361/202037588. arXiv: 2002.10895 [astro-ph.SR].

Nèmec, N. E. et al. (2023). "Forward modelling of brightness variations in Sun-like stars. II. Light curves and variability". In: *Astronomy & Astrophysics* 672, A138, A138. DOI: 10.1051/0004-6361/202244412. arXiv: 2303.03040 [astro-ph.SR].

Peixoto, Jose P. and Abraham H. Oort (1992). *Physics of climate*.

Pesnell, W. Dean, B. J. Thompson, and P. C. Chamberlin (2012). "The Solar Dynamics Observatory (SDO)". In: *Solar Physics* 275.1-2, pp. 3–15. DOI: 10.1007/s11207-011-9841-3.

Peter, Kerstin et al. (2014). "The dayside ionospheres of Mars and Venus: Comparing a one-dimensional photochemical model with MaRS (Mars Express) and VeRa (Venus Express) observations". In: *Icarus* 233, pp. 66–82. ISSN: 0019-1035. DOI: https://doi.org/10.1016/j.icarus.2014.01.028. URL: https://www.sciencedirect.com/science/article/pii/S0019103514000591.

Quémerais, Eric et al. (2019). "Multiple Scattering Effects in the Interplanetary Medium: Evaluation Using SOHO SWAN and MAVEN EUVM Lyman α Measurements". In: *Journal of Geophysical Research: Space Physics* 124.6, pp. 3949–3960. DOI: https://doi.org/10.1029/2019JA026674.

Ramstad, Robin et al. (2015). "The Martian atmospheric ion escape rate dependence on solar wind and solar EUV conditions: 1. Seven years of Mars Express observations". In: *Journal of Geophysical Research: Planets* 120.7, pp. 1298–1309. DOI: https://doi.org/10.1002/2015JE004816. eprint: https://agupubs.onlinelibrary.wiley.com/doi/pdf/10.1002/2015JE004816. URL: https://agupubs.onlinelibrary.wiley.com/doi/abs/10.1002/2015JE004816.

Rempel, Matthias and Rolf Schlichenmaier (2011). "Sunspot Modeling: From Simplified Models to Radiative MHD Simulations". In: *Living Reviews in Solar Physics* 8.1, 3, p. 3. DOI: 10.12942/lrsp-2011-3.

Schou, J. et al. (2012). "Design and Ground Calibration of the Helioseismic and Magnetic Imager (HMI) Instrument on the Solar Dynamics Observatory (SDO)". In: *Solar Physics* 275.1-2, pp. 229–259. DOI: 10.1007/s11207-011-9842-2.

Shapiro, A. I. et al. (2016). "Are solar brightness variations faculae- or spot-dominated?" In: *Astronomy & Astrophysics* 589, A46, A46. DOI: 10.1051/0004-6361/201527527. arXiv: 1602.04447 [astro-ph.SR].

Snow, Martin et al. (2005). "Solar Stellar Irradiance Comparison Experiment II (Solstice II): Examination of the Solar Stellar Comparison Technique". In: *Solar Physics* 230.1-2, pp. 295–324. DOI: 10.1007/s11207-005-8763-3.

Solanki, S. K. et al. (2020). "The Polarimetric and Helioseismic Imager on Solar Orbiter". In: *Astronomy & Astrophysics* 642, A11, A11. DOI: 10.1051/0004-6361/201935325. arXiv: 1903.11061 [astro-ph.IM].

Solanki, Sami K, Bernd Inhester, and Manfred Schüssler (2006). "The solar magnetic field". In: *Reports on Progress in Physics* 69.3, pp. 563–668. DOI: 10.1088/0034-4885/69/3/r02. URL: https://doi.org/10.1088/0034-4885/69/3/r02.

Solanki, Sami K., Natalie A. Krivova, and Joanna D. Haigh (2013). "Solar Irradiance Variability and Climate". In: *Annual Review of Astronomy and Astrophysics* 51.1, pp. 311–351. DOI: 10.1146/annurev-astro-082812-141007. arXiv: 1306.2770 [astro-ph.SR].

Sowmya, K. et al. (2021a). "Modeling Stellar Ca II H and K Emission Variations. I. Effect of Inclination on the S-index". In: *The Astrophysical Journal* 914.1, 21, p. 21. DOI: 10.3847/1538-4357/abf247. arXiv: 2103.13893 [astro-ph.SR].

Sowmya, K. et al. (2021b). "Predictions of Astrometric Jitter for Sun-like Stars. II. Dependence on Inclination, Metallicity, and Active-region Nesting". In: *The Astrophysical Journal* 919.2, 94, p. 94. DOI: 10.3847/1538-4357/ac111b. arXiv: 2107.01493 [astro-ph.SR].

Sowmya, K. et al. (2023). "Modeling Stellar Ca II H and K Emission Variations: Spot Contribution to the S-index". In: *The Astrophysical Journal Letters* 956.1, L10, p. L10. DOI: 10.3847/2041-8213/acf92a. arXiv: 2309.03690 [astro-ph.SR].

Spruit, H. C. (1976). "Pressure equilibrium and energy balance of small photospheric fluxtubes." In: *Solar Physics* 50.2, pp. 269–295. DOI: 10.1007/BF00155292.

Steiner, O. (2005). "Radiative properties of magnetic elements. II. Center to limb variation of the appearance of photospheric faculae". In: *Astronomy and Astrophysics* 430, pp. 691–700. DOI: 10.1051/0004-6361:20041286.

Tagirov, R. V. et al. (2019). "Readdressing the UV solar variability with SATIRE-S: non-LTE effects". In: *Astronomy & Astrophysics* 631, A178, A178. DOI: 10.1051/0004-6361/201935121. arXiv: 1909.11736 [astro-ph.SR].

Thiemann, E. et al. (2017). "The MAVEN EUVM model of solar spectral irradiance variability at Mars: Algorithms and results". In: *Journal of Geophysical Research: Space Physics* 122.3, pp. 2748–2767. DOI: https://doi.org/10.1002/2016JA023512. URL: https://agupubs.onlinelibrary.wiley.com/doi/abs/10.1002/2016JA023512.

Thiemann, E. et al. (2021). "Solar Extreme Ultraviolet Irradiance Uncertainties for Planetary Studies". In: *Journal of Geophysical Research: Space Physics* 126.1, e2020JA028184. DOI: https://doi.org/10.1029/2020JA028184. URL: https://agupubs.onlinelibrary.wiley.com/doi/abs/10.1029/2020JA028184.

Uitenbroek, H. (2001). "Multilevel Radiative Transfer with Partial Frequency Redistribution". In: *The Astrophysical Journal* 557.1, pp. 389–398. DOI: 10.1086/321659.

Unruh, Y. C., S. K. Solanki, and M. Fligge (1999). "The spectral dependence of facular contrast and solar irradiance variations". In: *Astronomy & Astrophysics* 345, pp. 635–642.

Vaughan, A. H., G. W. Preston, and O. C. Wilson (1978). "Flux measurements of Ca II and K emission." In: *Publications of the Astronomical Society of the Pacific* 90, pp. 267–274. DOI: 10.1086/130324.

Viereck, Rodney et al. (2001). "The Mg II index: A proxy for solar EUV". In: *Geophysical Research Letters* 28.7, pp. 1343–1346. DOI: https://doi.org/10.1029/2000GL012551. eprint: https://agupubs.onlinelibrary.wiley.com/doi/pdf/10.1029/2000GL012551. URL: https://agupubs.onlinelibrary.wiley.com/doi/abs/10.1029/2000GL012551.

Vourlidas, Angelos (2015). "Mission to the Sun-Earth L5 Lagrangian Point: An Optimal Platform for Space Weather Research". In: *Space Weather* 13.4, pp. 197–201. DOI: https://doi.org/10.1002/2015SW001173. eprint: https://agupubs.onlinelibrary.wiley.com/doi/pdf/10.1002/2015SW001173. URL: https://agupubs.onlinelibrary.wiley.com/doi/abs/10.1002/2015SW001173.

Wilson, O. C. (1978). "Chromospheric variations in main-sequence stars." In: *The Astrophysical Journal* 226, pp. 379–396. DOI: 10.1086/156618.

Yang, D. et al. (2023). "Direct assessment of SDO/HMI helioseismology of active regions on the Sun's far side using SO/PHI magnetograms". In: *Astronomy & Astrophysics* 674, A183. DOI: 10.1051/0004-6361/202346030. URL: https://doi.org/10.1051/0004-6361/202346030.

Yang, Dan, Laurent Gizon, and Hélène Barucq (2023). "Imaging individual active regions on the Sun's far side with improved helioseismic holography". In: *Astronomy & Astrophysics* 669, A89, A89. DOI: 10.1051/0004-6361/202244923. arXiv: 2211.07219 [astro-ph.SR].

Yang, Dan et al. (2024, in preparation). *Combined surface flux transport and helioseismic Far-side Active Region Model (FARM).*

Yeo, K. L. et al. (2014). "Reconstruction of total and spectral solar irradiance from 1974 to 2013 based on KPVT, SoHO/MDI, and SDO/HMI observations". In: *Astronomy & Astrophysics* 570, A85, A85. DOI: 10.1051/0004-6361/201423628. arXiv: 1408.1229 [astro-ph.SR].

Appendix to Chapter 4

This appendix presents the preliminary results of my efforts to estimate the area coverage of sunspots and faculae using magnetic field and intensity continuum data. The goal was to establish a relationship between the magnetic field and intensity continuum maps to predict the location of sunspots based solely on magnetic field information. Two approaches were employed.

Firstly, I analyzed the magnetic field as a function of the intensity continuum for each pixel of Gaussian-smoothed HMI data. The results for a single day are shown in Figure 1, and for 60 days (sampled every six days in 2014) with linear fits, in Figure 2.

Secondly, I employed neural networks and machine learning algorithms to detect patterns between the magnetic field and the intensity continuum. The aim was to use this empirical relationship to identify sunspot locations. However, I have not yet developed a model that accurately predicts sunspot locations from magnetic field data alone. Figure 3 compares the expected spot mask (top right) with the predicted spot mask (bottom left) generated by a neural network model. The model was trained using a Dice loss function with a learning rate of 0.0001 for 20 epochs.

These preliminary results lay the groundwork for developing a more sophisticated model that can estimate the area coverage of sunspots and faculae using only magnetic field data. While the current results are not yet precise enough for estimating solar irradiance variability, they show promise for future advancements in this area.

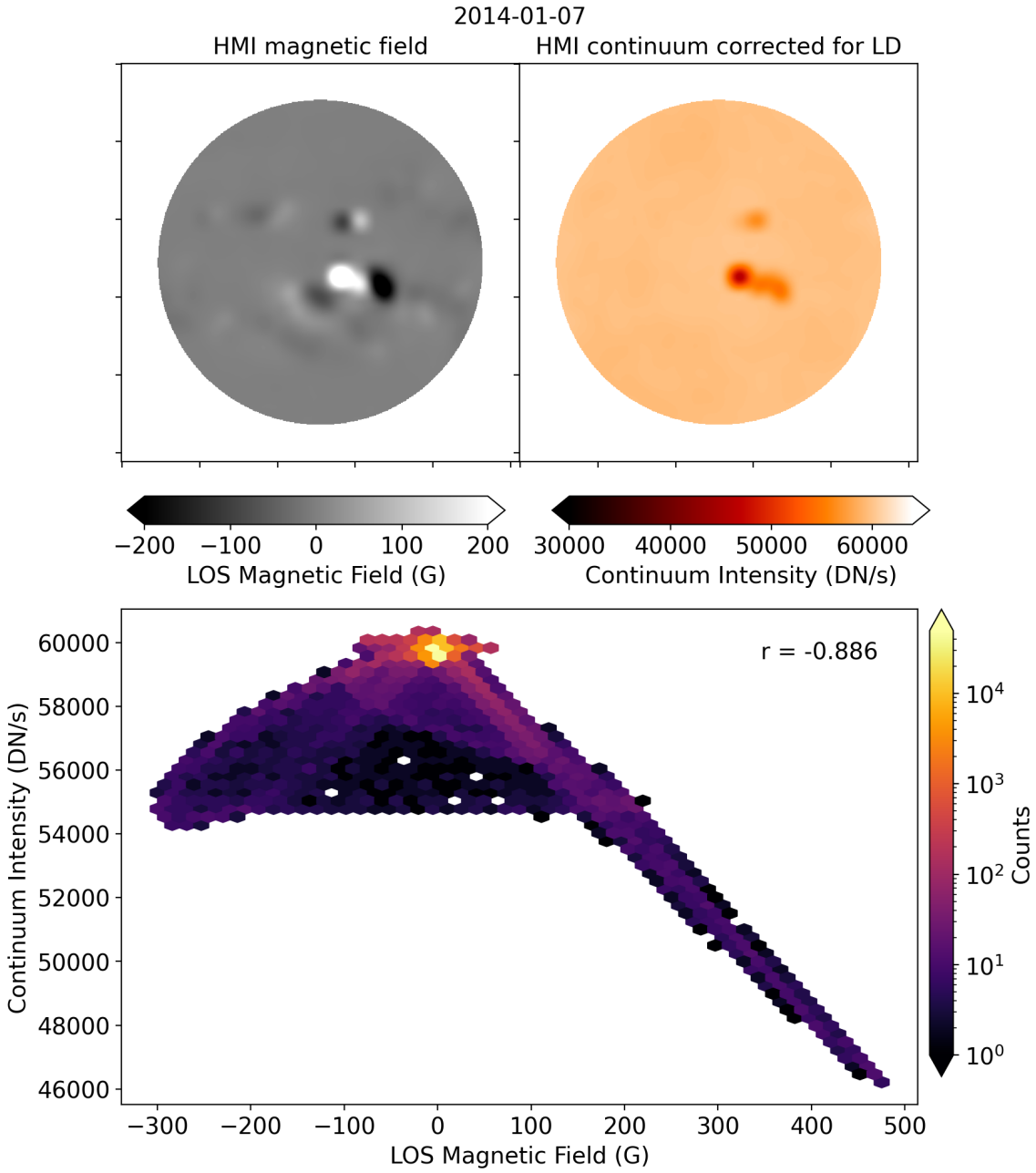

Figure 1: LOS magnetic field as a function of the intensity continuum (corrected for limb darkening) for January 7th, 2014. In both images, the limb regions was removed and a Gaussian filter was applied.

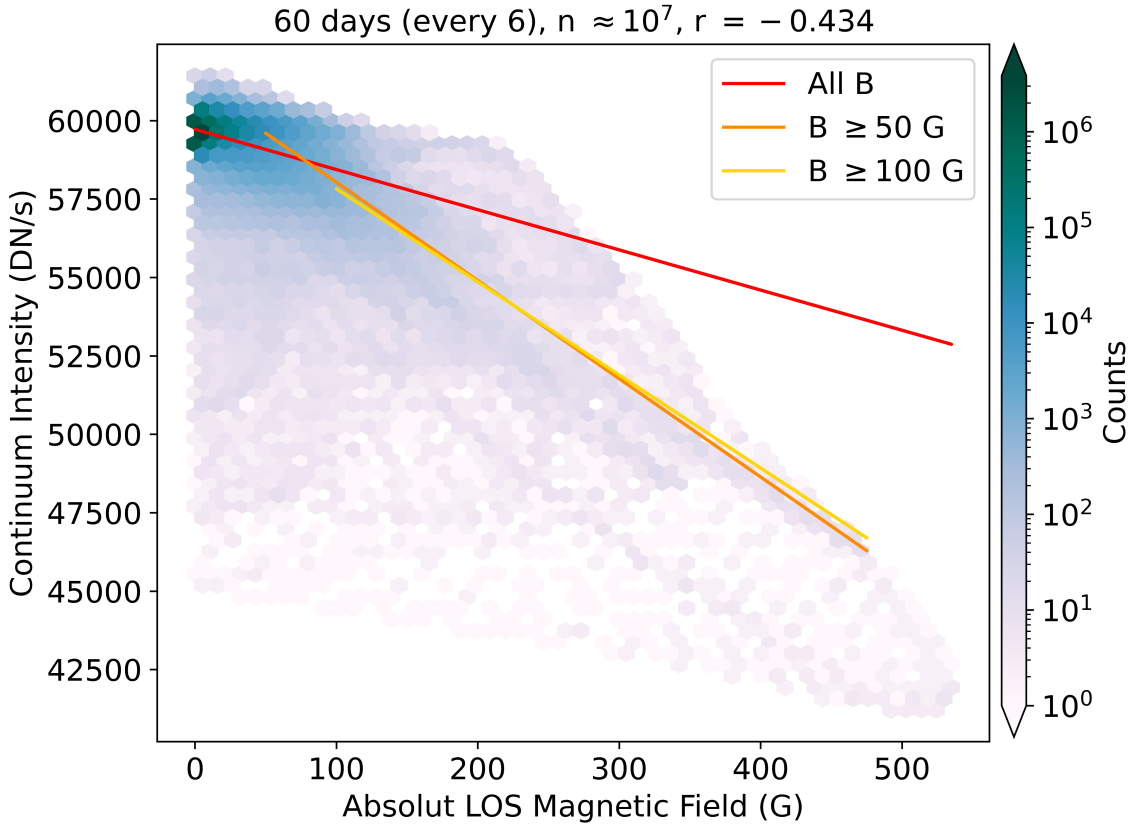

Figure 2: Absolute value of the magnetic field as a function of the intensity continuum for 60 days sampled every six days in 2014. The total number of pixels (n) and the correlation coefficient (r) of the data are provided at the top of the panel. Linear regressions for different magnetic field thresholds are shown in red, orange, and yellow lines.

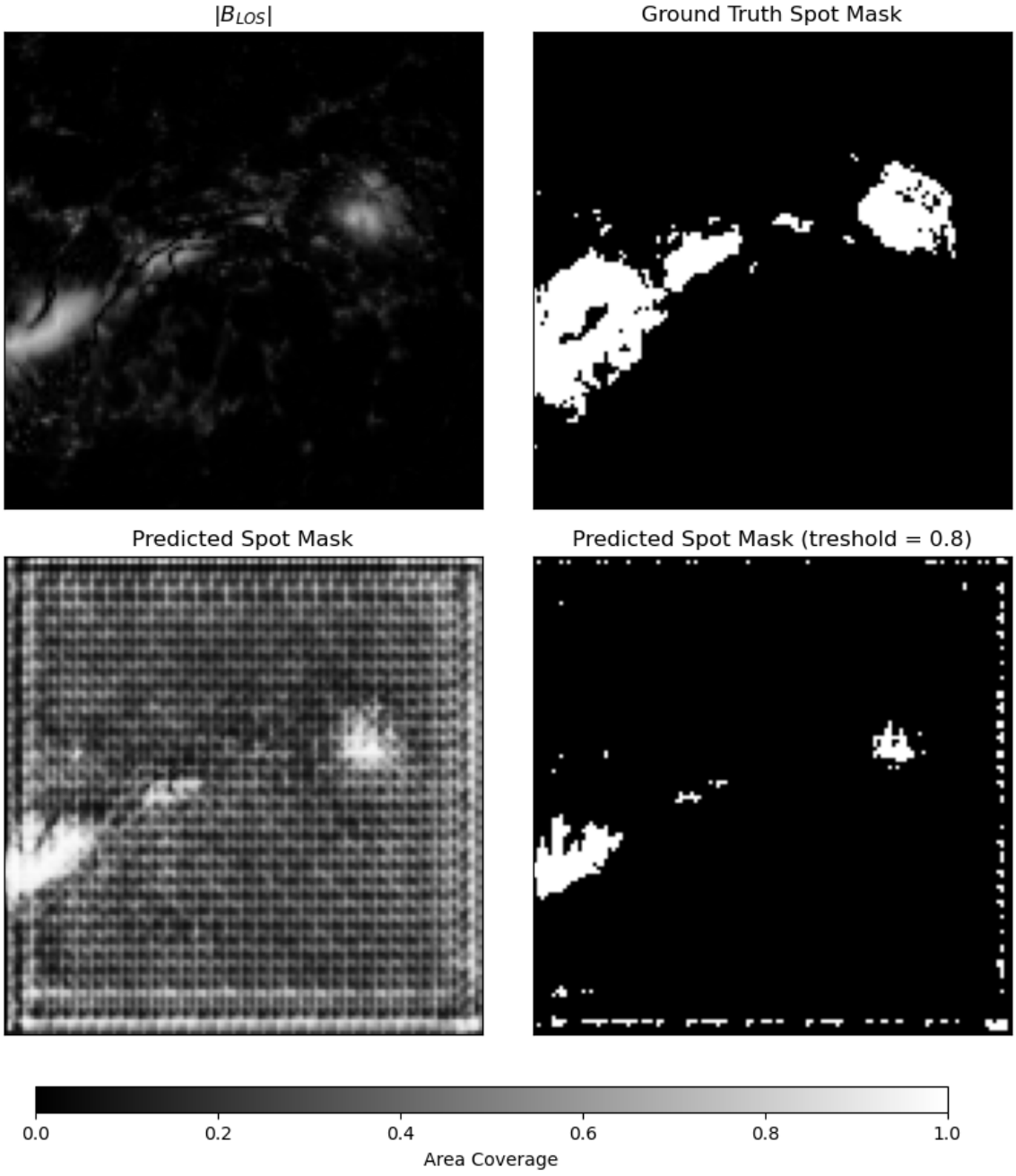

Figure 3: Example of a neural network model predicting sunspot locations from a small region in an HMI magnetogram. Top left: Absolute LOS magnetic field. Top right: Spot mask derived from the corresponding region in the intensity continuum map. Bottom left: Predicted spot mask from the neural network. Bottom right: Predicted mask thresholded at 0.8.

Acknowledgements

First of all, I would like to express my love for my husband, atmospheric physicist, and programming genius Dr. Richard Erik Larsson, who has been my safe harbour and my inspiration – and even my reviewer! – throughout this journey. I would not have been able to start or finish this dissertation without his support, his knowledge, his coding tips, and his unconditional love. I am forever grateful for everything you have done for me!

I would like to thank my friends and colleagues still at the Max Planck Institute for Solar System Research for their support and encouragement throughout this phase of my life – a special hooray to Abhiroop, Amanda, Borys, Dusan, Jonathan, Nikolina, and Ziwen. I have had very good times with all of you, and I will always cherish the memories we have created together. Please, don't ever let the daily coffee breaks and the weekly Friday's Beers end!

To my friends outside the institute – Alexandra, Argiris, Gabrielle, Karlita, Kok Leng, Larissa, Mariana, Sebastian – I would like to express my love and gratitude for being there for me, for listening to me, and for making me laugh when I needed it the most. I am very grateful for having you in my life!

To my friends in the MegaGauss band – Guillaume, Johannes, Lisa-Marie, Paula, Prithwitosh, Sanghita, Tanayveer, Valera, Vignesh, Yara – I would like to thank for the good times we have had together, for the music we have played, and for the gigs we have performed. I will never forget the fun we have had!

To my office mates – Illya and Rody – I would like to thank for putting (non-intentional) pressure on me to finish this dissertation. It is indeed very embarrassing to lazily sit in the office while you are working hard on your projects. I wish you had arrived sooner so that I would have produced more papers!

I would like to express my deepest gratitude to my daily supervisors – Dr. Alexander Shapiro and Dr. Dan Yang – and to my co-authors – Dr. Nina-Elizabeth Nèmec and Dr. Sowmya Krishnamurthy – for their guidance, support, and knowledge-sharing throughout this research. Their expertise have been invaluable to me, and I am very grateful for having them as my mentors and co-authors.

I would like to thank my formal supervisor and funder, Prof. Dr. Laurent Gizon, for giving me the opportunity of working in a PhD project in his department. I would also like to thank the members of the Thesis Committee for their time and effort in reviewing this dissertation.

I would like to thank Dr. Sonja Schuh and Johanna Wagner-Farssi, who are in charge of the International Max Planck Research School (IMPRS) for Solar System Science at the University of Göttingen. I am very grateful for their support and for the opportunities they have provided me during my time as a PhD student. I would also like to thank the administration and technical staff at my institute for being always willing to help me figure out stuff.

I would like to thank Dr. Dimitra Atri and Dr. Dattaraj Dhuri for welcoming me as a guest researcher at the Center for Space Science at the New York University of Abu Dhabi. I have had a productive and inspiring time working with you, and I am very grateful for the opportunity given to me to meet the Emirates Mars Mission Science Team in person.

I would like to thank Prof. Dr. Stefan Bühler and his team at the Meteorological Institute of the University of Hamburg for welcoming me as a guest researcher during my mobile work in Hamburg. I have been always very productive when working in a shared office with my husband, and I am very grateful for the opportunity of working in such a nice environment.

I would like to thank Dr. Samarth Kashyap for initiating me in the world of neural networks and for providing me with the tools to start my journey in machine learning. I am very grateful for his patience and for his willingness to help me whenever I needed it. I really enjoyed building those neural networks!

At last but definitely not least, I would like to properly acknowledge the developers of the software that I have used to gather, analyze, and visualize the data presented in this dissertation: Python, Matplotlib, NumPy, SciPy, Pandas, AstroPy, SunPy, and JHelioviewer. I would also like to thank the developers of Visual Studio Code, which I have used to write my scripts and the dissertation itself, and to GitHub Copilot, which has literally read my mind several times and has become my best coding buddy. I will never forget you, GitHub Copilot!